J. Fluid Mech. (2010), *vol.* 653, *pp.* 1–33. © Cambridge University Press 2010
doi:10.1017/S0022112010000133

Thermoacoustic instability in a solid rocket motor: non-normality and nonlinear instabilities

SATHESH MARIAPPAN AND R. I. SUJITH†

Department of Aerospace Engineering, Indian Institute of Technology Madras, Chennai 600036, India

(Received 20 May 2009; revised 31 December 2009; accepted 4 January 2010;
first published online 27 April 2010)

An analytical framework is developed to understand and predict the thermoacoustic instability in solid rocket motors, taking into account the non-orthogonality of the eigenmodes of the unsteady coupled system. The coupled system comprises the dynamics of the acoustic field and the propellant burn rate. In general, thermoacoustic systems are non-normal leading to non-orthogonality of the eigenmodes. For such systems, the classical linear stability predicted from the eigenvalue analysis is valid in the asymptotic (large time) limit. However, the short-term dynamics can be completely different and a generalized stability theory is needed to predict the linear stability for all times. Non-normal systems show an initial transient growth for suitable initial perturbations even when the system is stable according to the classical linear stability theory. The terms contributing to the non-normality in the acoustic field and unsteady burn rate equations are identified. These terms, which were neglected in the earlier analyses, are incorporated in this analysis. Furthermore, the short-term dynamics are analysed using a system of differential equations that couples the acoustic field and the burn rate, rather than using *ad hoc* response functions which were used in earlier analyses. In this paper, a solid rocket motor with homogeneous propellant grain has been analysed. Modelling the evolution of the unsteady burn rate using a differential equation increases the degrees of freedom of the thermoacoustic system. Hence, a new generalized disturbance energy is defined which measures the growth and decay of the oscillations. This disturbance energy includes both acoustic energy and unsteady energy in the propellant and is used to quantify the transient growth in the system. Nonlinearities in the system are incorporated by including second-order acoustics and a physics-based nonlinear unsteady burn rate model. Nonlinear instabilities are analysed with special attention given to 'pulsed instability'. Pulsed instability is shown to occur with pressure coupling for burn rate response. Transient growth is shown to play an important role in pulsed instability.

1. Introduction

Solid rocket motors (SRMs) are often prone to combustion instability. The prediction of combustion instability in the early stage of the design is a formidable task due to the complex unsteady flow field existing in the combustion chamber. Combustion instability occurs when the unsteady burn rate from the propellant (in SRMs) is amplified by the positive feedback of the acoustic oscillations in the chamber. Combustion instability causes excessive pressure oscillations, which might resonate with the structural modes of the rocket, leading to excessive vibration

† Email address for correspondence: sujith@iitm.ac.in

https://doi.org/10.1017/S0022112010000133 Published online by Cambridge University Press

and damage of the payload. Furthermore, during the occurrence of the combustion instability, the heat transfer to the combustion chamber walls is increased, eventually melting them (Sutton 2001). Instabilities in SRMs have been known to exist since 1930 (Culick 2006). Since then, many investigations were conducted to understand the mechanisms behind them and to arrive at measures to control the same. Furthermore, combustion instability alone is not the only source of instability in an SRM. Although other instabilities such as chuffing or L^* instability (Sutton 2001), acoustic instability due to vortex shedding in segmented motors (Vuillot 1995; Kourta 1997; Anthoine, Buchlin & Hirschberg 2002) and instability of shear waves at the propellant surface (Flandro & Majdalani 2003) are important, this paper focuses only on the thermoacoustic instabilities in the SRM. In the SRM, the driving mechanism for combustion instability to happen is the response of the unsteady burn rate of the propellant to chamber acoustics. This leads to unsteady mass addition to the combustion chamber and ultimately causes an unsteady heat release rate.

Thermoacoustic instabilities in SRMs are attributed to the time lag between the unsteady burn rate and the chamber acoustics. The phase delay for a particular frequency can be identified in the time domain as a 'time lag'. The physical origin of this time lag can be attributed to various dynamical processes involved in the burn rate dynamics of the propellant. Instability occurs if the time lag is in some suitable range such that fluctuating energy is added to the system. The above idea gave rise to the $n-\tau$ model (n is the interaction index that gives the coupling strength between the acoustic velocity and the unsteady combustion process and τ is the time lag) developed by Crocco (1956) for liquid rocket engines. The model was very simple; n and τ vary with frequency in realistic situations. However, it gave a basic understanding of the physical origin of instability.

Initial attempts to tackle the instabilities theoretically were by Culick (1963) and Friedly & Peterson (1966), where the linearized equations were studied. They obtained an explicit expression for the complex frequency of the system. The real part of the frequency gave the growth or decay of the oscillations. Because the unsteady heat release rate was the main driving source for the acoustic oscillations, a relation between the two was developed in order to characterize the system dynamics. This coupling between the unsteady burn rate in response to acoustic oscillation was captured by the frequency-dependent admittance function ($Y = M_b[(m'/\bar{m})/(p'/\gamma\bar{p}) - (\rho'/\bar{\rho})/(p'/\gamma\bar{p})]$) described by Culick (1968), where M_b denotes the Mach number at the burning surface, m is the mass addition rate, p is the pressure and ρ is the density. The prime ($'$) denotes fluctuating quantities, while the overbar ($\bar{}$) denotes mean quantities. The admittance function calculated was used to determine the growth of the acoustic oscillations. Analytical expressions for the admittance function in the linear regime were derived by Williams (1962) and Deluca, Disilvestro & Cozzi (1995). The governing equations are nonlinear partial differential equations for the burn rate, which makes the problem difficult to solve for composite propellants. Some semi-empirical theories were proposed to handle these difficulties (Brewster & Son 1995). The form of the admittance function was derived and its exact parameters were found experimentally (Price 1984). One of the successful experimental techniques used to calculate the parameter values was the T-burner technique (from the admittance function), which was demonstrated by Lin & Wang (1995). Experimental and theoretical analyses were used in tandem to predict instabilities.

A theoretical analysis starts with linearizing the governing equations and analysing their stability. This leads to finding the eigenvalues (complex frequency) and eigenmodes of the system. In a classical linear stability analysis, a system is said

https://doi.org/10.1017/S0022112010000133 Published online by Cambridge University Press

to be linearly stable if the oscillations decay to zero in the asymptotic time limit, reaching finally the steady state (stable fixed point). The system is linearly unstable if the oscillations grow exponentially. Both the definitions are for 'small' disturbances with respect to the corresponding mean quantities. The stability of the system is determined by the real part of the eigenvalues as described earlier. A linearly unstable system grows exponentially, and after some time the oscillation amplitudes are not small. The nonlinear effects start playing a major role in the time evolution of the system, causing the evolution to reach a limit cycle (oscillations with constant amplitude). This nonlinearity is attributed to the nonlinear chamber acoustics and nonlinear combustion response of the propellant (Culick 2006).

Culick (1976*a*) was the first to derive an analytical condition for the existence of stable and unique limit cycle behaviour using a two-mode Galerkin approximation with second-order acoustics as the only nonlinear process. Nonlinearity in the combustion response was also included in the analysis and the dynamical behaviour was analysed (Levine & Baum 1983; Flandro, Fischbach & Majdalani 2007). Apart from these, the effect of particulate damping (Culick 1976*b*), vorticity (Flandro 1995*a*) and flow turning (Flandro 1995*b*) on SRM stability was discussed. Computational fluid dynamics (CFD) analysis was performed by Schimada *et al.* (2007) using the admittance function for burn rate–acoustic coupling and quasi-steady flame model in the gas phase. Growth rates at low Mach numbers were predicted more accurately by a second-order finite volume method than the Galerkin technique usually used for such analysis (Culick 2006).

Another interesting dynamical behaviour observed experimentally was that SRMs stable for small-amplitude disturbances were seen to become unstable for larger ones (Culick 2006). This was called 'pulsed instability' or 'triggering'. Many mechanisms have been proposed for explaining triggering in the past. Second-order gas dynamics alone were proved to be insufficient to cause triggering because of the absence of 'self-coupling' terms (Culick 1994). Higher-order gas dynamics (third-order acoustics) also proved the same (Yang, Kim & Culick 1990). Hence, a nonlinear combustion response was thought of as an alternative candidate for triggering. Culick, Burnley & Swenson (1995) used an *ad hoc* nonlinear velocity coupling model for burn rate response to show triggering numerically. Wicker *et al.* (1996) analysed various forms of nonlinear coupling between unsteady burn rate and acoustic variables. By suitably adjusting the parameters and the form of the coupling terms, triggering was demonstrated. Anathakrishnan, Deo & Culick (2005) further explained that velocity-coupled models are the only possible candidates for causing triggering in realistic operating regimes of SRMs.

In all the above analyses, there are some common assumptions and procedures that were adopted to solve the thermoacoustic instability problem in the SRM. They are (i) the orthogonality of the eigenmodes, (ii) the use of admittance (response) functions or *ad hoc* models for burn rate–acoustic coupling and (iii) the use of the classical linear stability theory for all time t. Culick (1997) showed that the frequency shift due to the non-orthogonality of the eigenmodes is second order in a mean flow Mach number. However, the system dynamics change dramatically during the initial time because of the non-orthogonality of the eigenmodes (Kedia, Nagaraja & Sujith 2008). The use of admittance (response) functions or *ad hoc* coupling models for burn rate–acoustic coupling does not account for the initial transients in the burn rate. These can lead to erroneous prediction of the system dynamics, both qualitatively and quantitatively. If the evolution of the unsteady propellant burn rate is modelled using a differential equation in time, then the degrees of freedom for the system are increased. This

https://doi.org/10.1017/S0022112010000133 Published online by Cambridge University Press

implies that the thermoacoustic system variables include not only acoustic pressure and velocity but also other variables related to the unsteady burn rate. Therefore, the initial condition on the problem is restricted not only to acoustic variables but also to unsteady burn rate, which might show an interesting behaviour. Indeed, it is found that the effects of non-orthogonality of the eigenmodes play an important role in the initial conditions related to the unsteady burn rate. The last assumption, i.e. the validity of the classical linear stability theory, is applicable only in the asymptotic time limit (Strogatz 2001). This assumption is valid during the initial period, only if the eigenmodes are orthogonal to each other. Therefore, a new generalized stability criterion (Farrell & Ioannou 1996) has to be used to account for the short-term dynamics. This paper relaxes the above three assumptions and offers a more complete analysis of the thermoacoustic instability in the SRM. A homogeneous propellant is considered for the present analysis.

2. Non-normality and transient growth

A system is said to be non-normal if the linear operator L governing the system evolution does not commute with its adjoint $L^\dagger$ ($LL^\dagger \neq L^\dagger L$, $\dagger$ indicates an adjoint operator) (Golub & Van Loan 1989). For such systems, the eigenmodes (eigenvectors) are non-orthogonal. Any initial condition for the system can be written as a linear combination of the eigenmodes. For a linearized system, stable under the classical linear stability (no nonlinearities included), all eigenmodes are decaying monotonically in time. However, in the case of the non-normal system, the vectorial sum of the eigenmodes which gives the state of the system at any time t can increase (for a suitable initial condition) for a short time and eventually decays after a long time (Schmid & Henningson 2001). The transient growth occurring might be of several orders of magnitude and the system might reach a different dynamical behaviour, e.g. limit cycles, if the nonlinearities become significant as the amplitude increases during this growth (Balasubramanian & Sujith 2008*a*). The qualitative change in the dynamical behaviour due to transient growth cannot be predicted by the classical linear stability theory, which studies the stability of individual eigenmodes and analyses the spectrum in the complex plane. However, the orthogonality of the eigenmodes was explicitly assumed in previous analyses of thermoacoustic systems (Culick 1997, 2006). It has been shown recently that thermoacoustic systems are non-normal in general, and the consequences of non-normality are discussed in the context of ducted diffusion flames (Balasubramanian & Sujith 2008*a*) and the Rijke tube (Balasubramanian & Sujith 2008*b*). In fluid flows, the interplay between non-normality and nonlinearity is shown to be one of the routes for the sub-critical transition to turbulence (Gebgart & Grossmann 1994; Baggett, Driscoll & Trefethen 1995; Barkley & Tuckerman 1999; Criminale & Drazin 2000). An excellent review of non-orthogonality of the eigenmodes and its effects on transient growth in the context of the stability of laminar shear flows is given by Schmid (2007). Non-normality and transient growth are observed in many areas of research including magnetohydrodynamics (Krasnov *et al.* 2004), astrophysics (Mukhopadhyay, Afshordi & Narayan 2006) and atmospheric flows (Farrell & Ioannou, 1996).

In the past, linear stability analyses of SRMs were performed using the classical linear stability theory (Culick 2006). Energy in the eigenmodes can be transferred from one eigenmode to another, either due to nonlinear coupling (Culick 1976*a*) or due to non-orthogonality of the eigenmodes (Balasubramanian & Sujith 2008*b*). In the former case, the coupling comes from the nonlinear time evolution equation for

https://doi.org/10.1017/S0022112010000133 Published online by Cambridge University Press

the eigenmodes. This is a 'direct interaction'. This requires some threshold amplitude (system dependent) to be reached for it to have significant effects in the dynamical evolution of the system. In the latter case, the energy transfer occurs even with small disturbances. In this limit, the nonlinearity present in the system (which will have a mild effect at small amplitudes) transfers a small amount of energy from one eigenmode to another. If the energy transfer leads to a distribution of energy among the modes in such a way that transient growth happens, there is a net energy transfer from the base flow to the eigenmodes. For a linearly stable case, the energy given in one eigenmode is fed to the base flow and from it the energy is fed back again to other eigenmodes. Thus, energy transfer happens through the base flow. It is an 'indirect interaction'.

It is evident that the stability analysis of the SRM has to be modified including considering the non-orthogonality of eigenmodes. The phenomenon of pulsed instability observed in SRMs has been demonstrated theoretically only with *ad hoc* burn rate–acoustic coupling models. This paper concentrates on the four main issues. The first issue is the inclusion of the non-orthogonality of eigenmodes, which plays an important role in the short-term dynamics of the system. The second is to use a physics-based model for the burn rate response of a homogeneous propellant to demonstrate the various observed phenomena, especially pulsed instability. The model also captures the transients (important for non-normal systems), which facilitates the prediction of system dynamics during the initial time. Therefore, a differential equation for the time evolution of the state vector is derived for the unsteady burn rate–acoustic coupling and is solved simultaneously along with the equations for the acoustic field. The dynamical system now considered comprises not only acoustic variables (with a source from the unsteady propellant burn rate) but also the variables associated with the unsteady burn rate. The third issue is to include all the nonlinear processes involved, so that the energy transfer and large amplitude oscillations (limit cycles) are accurately predicted. The fourth issue is that experiments performed by Blomshield *et al.* (1997*b*) indicate that the triggering pressure amplitude required for pulsed instability is very small (see figure 13 and table 5 of Blomshield *et al.* 1997*b*) compared to the steady state and mean pressure during the limit cycle (triggering pressure amplitude is $\sim$4 % of the steady state pressure). Furthermore, the triggering pressure amplitude in their study is much smaller than the limit cycle amplitude. This paper investigates if pulsed instability can be obtained from a small-amplitude initial pulse (compared with the limit cycle amplitude) as observed by Blomshield *et al.* (1997*b*).

3. Formulation

The SRM considered here has a prismatic cylindrical propellant grain of length l, port circumference S_l and a constant port area S_c. A schematic of the geometry considered with the coordinate system used is shown in figure 1. A cylindrical geometry is studied so as to make the analysis simple.

3.1. *Chamber acoustics*

In the SRM, the amplitude of the limit cycle pressure oscillations is often about 20 % of the mean chamber pressure (Culick 1976*a*; Flandro 1996). In this range of pressure oscillations, nonlinear acoustics plays an important role in the nonlinear dynamical evolution of the system. This is in contrast to gas turbines, where the limit cycle pressure oscillations are 3 %–4 % of the mean chamber pressure (Lee & Santavicca 2005) and the nonlinearity in combustion response alone can

https://doi.org/10.1017/S0022112010000133 Published online by Cambridge University Press

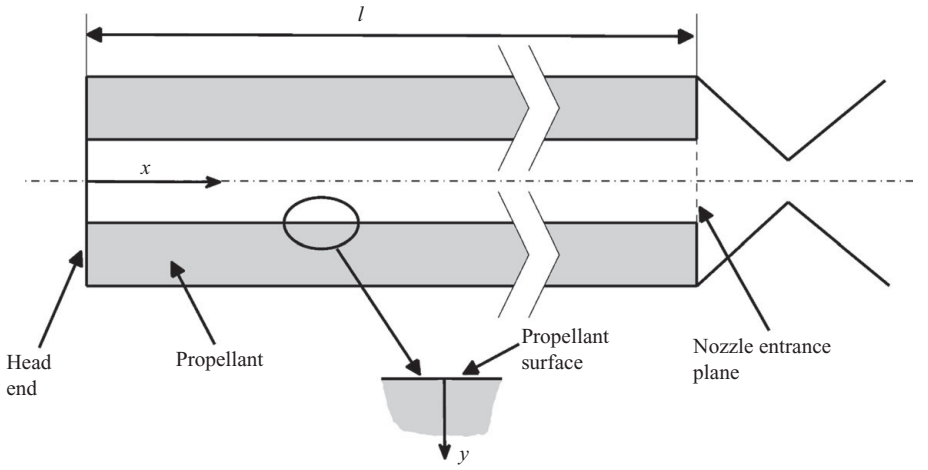


FIGURE 1. Schematic diagram of the combustion chamber geometry of the SRM considered.

be assumed to play an important role. Hence the present analysis includes a second-order nonlinearity in acoustics (Culick 1976*a*, 1976*b*, 1994; Yang *et al.* 1990) and a physics-based nonlinear model for combustion response (Krier *et al.* 1968). The acoustic oscillations are assumed to be isentropic, which is valid up to the inclusion of second-order nonlinearities (Culick 1997). Reddy & Trefethen (1994) have shown that the convection differential operator causes non-normality in the system ($(\mathrm{d}/\mathrm{d}x)^{\dagger} = -\mathrm{d}/\mathrm{d}x$, $\dagger$ indicates adjoint operator). Therefore, the stronger the convection, the higher is the level of non-normality. In SRM combustion chambers, the mean flow Mach number is around 0.1, which creates strong convective effects. Hence, the distribution of mean axial velocity plays a key role in characterizing the non-normality of the system. The above picture can be looked as an asymmetry in the flow field, which eventually leads to non-normality. A similar kind of asymmetry is present in the earlier analysis with a diffusion flame (Balasubramanian & Sujith 2008*a*) and Rijke tube (Balasubramanian & Sujith 2008*b*) due to the presence of a localized heat source. In contrast to these, an SRM has distributed heat sources; however, the strong convection leaves the system non-normal. In general, non-normality in a convection–diffusion problem occurs from the convection term that creates asymmetry in the distribution of any flow variable because of the directionality of the base flow, whereas diffusion is a gradual process which does not create any asymmetry (Balasubramanian & Sujith 2008*a*). In order to keep the analysis tractable, we assume a constant mean chamber pressure $\bar{p}$, density $\bar{\rho}$ and temperature $\bar{T}$, which are valid assumptions for an SRM (Culick 1997). The effects of 'flow turning' (stabilizing) and 'pumping' (destabilizing) cancel each other exactly for cylindrical propellant geometry (Flandro 1995*b*); hence, they do not appear in this analysis. The one-dimensional steady continuity equation is

$$\frac{\partial(\bar{\rho}\bar{u})}{\partial\tilde{x}} = \bar{m} \quad \text{and} \quad \bar{m} = \bar{R}\rho_p \frac{S_l}{S_c}, \tag{1}$$

where, $\bar{m}$ is the mean mass influx rate from the propellant per unit volume at any axial location, $\bar{u}$ is the base flow velocity, $\bar{R}$ is the mean propellant regression rate and ρ_p is

https://doi.org/10.1017/S0022112010000133 Published online by Cambridge University Press

the propellant density. Integrating the equation with head end velocity as zero gives

$$\bar{u} = \frac{\bar{m}}{\bar{\rho}}\tilde{x}. \tag{2}$$

The above equation gives the axial variation of mean velocity, which is used for further calculations. At low Mach numbers M, the isentropic relation for fluctuations in density can be used up to second-order acoustics (Culick 1976*a*). Hence, the continuity equation is decoupled from momentum and energy equations. The unsteady momentum and energy equations are given by

$$\widehat{\rho}\left(\frac{\partial \widehat{u}}{\partial \tilde{t}} + \widehat{u}\frac{\partial \widehat{u}}{\partial \tilde{x}}\right) = -\frac{\partial \widehat{p}}{\partial \tilde{t}} - \widehat{m}\widehat{u}, \tag{3}$$

$$\left(\frac{\partial \widehat{p}}{\partial \tilde{t}} + \widehat{u}\frac{\partial \widehat{p}}{\partial \tilde{x}} + \gamma \widehat{p}\frac{\partial \widehat{u}}{\partial \tilde{x}}\right) = (\gamma - 1)\widehat{Q}, \tag{4}$$

where $\widehat{m} = \widehat{R}\rho_p S_l/S_c$, $\widehat{Q} = \widehat{m}\Delta h$, Δh is the heat of reaction of the propellant at a constant pressure per unit mass and γ is the ratio of specific heat capacities at constant pressure and volume. The source term $\widehat{m}\widehat{u}$ in (3) is due to the reduction of the momentum of the fluid in the chamber due to the low-velocity inflow of the burning propellant. The source term $\widehat{Q}$ in (4) is due to the energy released by the propellant to the fluid in the chamber. Decomposing the flow variables as $\widehat{u} = \bar{u} + \tilde{u}'$, $\widehat{p} = \bar{p} + \tilde{p}'$, $\widehat{m} = \bar{m} + \tilde{m}'$, $\widehat{Q} = \bar{Q} + \tilde{Q}'$ and $\widehat{R} = \bar{R} + \tilde{R}'$, followed by substituting the above in (3) and (4), one obtains the governing equations for the perturbations. The acoustic momentum and energy equations thus obtained are (with nonlinear terms given within curly brackets $\{\}$):

$$\bar{\rho}\left[\frac{\partial \tilde{u}'}{\partial \tilde{t}} + \bar{u}\frac{\partial \tilde{u}'}{\partial \tilde{x}} + \tilde{u}'\frac{\mathrm{d}\bar{u}}{\mathrm{d}\tilde{x}}\right] + \left\{\bar{\rho}\tilde{u}'\frac{\partial \tilde{u}'}{\partial \tilde{x}} - \tilde{\rho}'\frac{\partial \tilde{p}'}{\partial \tilde{x}}\right\} = -\frac{\partial \tilde{p}'}{\partial \tilde{x}} - [\tilde{m}'\bar{u} + \bar{m}\tilde{u}' + \{\tilde{m}'\tilde{u}'\}], \tag{5}$$

$$\frac{\partial \tilde{p}'}{\partial \tilde{t}} + \bar{u}\frac{\partial \tilde{p}'}{\partial \tilde{x}} + \gamma\left[\bar{p}\frac{\partial \tilde{u}'}{\partial \tilde{x}} + \tilde{p}'\frac{\mathrm{d}\bar{u}}{\mathrm{d}\tilde{x}}\right] + \left\{\tilde{u}'\frac{\partial \tilde{p}'}{\partial \tilde{x}} + \gamma\tilde{p}'\frac{\partial \tilde{u}'}{\partial \tilde{x}}\right\} = (\gamma - 1)\widetilde{Q}', \tag{6}$$

where $\tilde{Q}' = \tilde{m}'\Delta h = \tilde{R}'\rho_p \Delta h(S_l/S_c)$, the tilde ($\sim$) denotes dimensional quantities, $\tilde{u}'$ is the acoustic velocity, $\tilde{p}'$ is the acoustic pressure, $\tilde{m}'$ is the fluctuation in mass influx rate per unit volume, $\tilde{Q}'$ is the fluctuating heat release rate per unit volume by the propellant combustion and $\tilde{R}'$ is the fluctuating burn rate.

We non-dimensionalize the above equations as follows: $p = \tilde{p}'/\bar{p}$, $u = \tilde{u}'/u_m$, $\bar{U} = \bar{u}/u_m$, $R = \tilde{R}'/\bar{R}$, $x = \tilde{x}/l$, $M = u_m/a$, where $u_m = (\bar{m}l)/(2\bar{\rho})$ is the average base flow velocity, $\bar{U} = 2x$ is the non-dimensional base flow velocity, a is the sonic speed and M is the average base flow Mach number. The non-dimensionalized acoustic momentum and energy equations are

$$\frac{\partial u}{\partial t} + M\left[\bar{U}\frac{\partial u}{\partial x} + \frac{\mathrm{d}U}{\mathrm{d}x}u\right] + \frac{1}{\gamma M}\frac{\partial p}{\partial x} = k_m[R\bar{U} + u] + \left\{k_m Ru - Mu\frac{\partial u}{\partial x} + \frac{p}{\gamma M}\frac{\partial p}{\partial x}\right\}, \tag{7}$$

$$\frac{\partial p}{\partial t} + \gamma M\left[\frac{\partial u}{\partial x} + \frac{\mathrm{d}\bar{U}}{\mathrm{d}x}p\right] + M\bar{U}\frac{\partial p}{\partial x} = k_e R - \left\{Mu\frac{\partial p}{\partial x} + \gamma Mp\frac{\partial u}{\partial x}\right\}, \tag{8}$$

where $k_m = -(\bar{m}u_m l)/(\bar{p}\gamma M)$, $k_e = ((\gamma - 1)l\bar{m}\Delta h)/(\bar{p}a)$.

https://doi.org/10.1017/S0022112010000133 Published online by Cambridge University Press

3.2. *Solution procedure*

The Galerkin technique (Zinn & Lores 1971; Padmanabhan 1975) is used to solve (7) and (8). The dependent variable is expanded as a linear combination of basis functions, which are chosen to satisfy the boundary conditions. The basis functions are chosen for a duct, which is acoustically closed at both ends, in spite of the non-zero admittance at the nozzle entry. The actual eigenmode shape is shown to deviate from the above, which is of the order of average mean flow Mach number ($M \sim 0.1$) (Culick 1976*a*). Although non-trivial boundary conditions lead to the non-normality of the system (Nicoud *et al.* 2007), our investigation mainly focuses on the non-normal nature of the system, arising purely from the interaction of chamber acoustics and unsteady burn rate. This can be regarded as the first step in analysing the non-normal nature of the thermoacoustic interaction in the SRM. Hereafter, the term 'mode' specifies only the Galerkin mode unless specified. The spatial distribution of the unsteady burn rate is expanded on the above basis. The coefficients R_m^c and R_m^s are obtained from the unsteady burn rate equation discussed in § 3.4. The variables are expanded as follows:

$$\left.\begin{aligned} u(x,t) = \sum_{m=1}^{N} U_m(t)\sin(\omega_m x), \quad p(x,t) = \gamma M \sum_{m=1}^{N} P_m(t)\cos(\omega_m x), \\ R(x,t) = \sum_{m=1}^{N} \left[R_m^c(t)\cos(\omega_m x) + R_m^s(t)\sin(\omega_m x)\right], \quad \omega_m = m\pi, \end{aligned}\right\} \tag{9}$$

where N is the number of Galerkin modes used in the above expansion. The above expressions are substituted in (7) and (8). Then the evolution of the coefficients (U_m, P_m, R_m^c and R_m^s) is obtained by projecting the obtained equation onto the basis function (Galerkin mode) used for expansion, utilizing the orthogonality of the basis function. The following evolution equations are finally obtained:

$$\dot{U}_n + 2\sum_{m=1}^{N}\left(U_m I_{n,m}^1 + P_m I_{n,m}^2 + R_m^c I_{n,m}^3 + R_m^s I_{n,m}^4\right) = 2\left\{k_m N_n^1 - M N_n^2 - \gamma N_n^3\right\}, \tag{10}$$

$$\dot{P}_n + \frac{2}{\gamma M}\left(\sum_{m=1}^{N}\left[U_m I_{n,m}^5 + P_m I_{n,m}^6 + R_m^c I_{n,m}^7\right]\right) = \frac{2}{\gamma M}\left\{\gamma M^2 N_n^4 - (\gamma M)^2 N_n^5\right\}. \tag{11}$$

The coupling terms are given in Appendix A.

The set of $2N$ coupled first-order ordinary differential equations is solved by using the fourth-order Runge–Kutta scheme (Riley, Hobson & Bence 2006). The integrals $I_{n,m}^1$, $I_{n,m}^3$ and $I_{n,m}^4$ are the major contributors for the non-normality of the system. The terms contain the convective term $\bar{U} = 2x$, which is a linear function of x giving a non-vanishing coupling integral. Thus, the coupling among the Galerkin modes is formed and termed as 'apparent linear coupling'. These terms lead to the initial transient growth and its relation to eigenmodes is discussed by Kedia *et al.* (2008). Note that the mean flow velocity $\bar{U} = 2x$ creates asymmetry in the flow field as discussed in § 3.1.

3.3. *Damping*

Nozzle damping and viscous dissipation are the sources of damping of acoustic oscillations in SRMs. The former contributes much to the damping of acoustic waves. A part of the incident wave at the choked nozzle is carried away by the mean flow (the remaining is reflected at the choked throat). Thus, some part of the acoustic energy is carried away from the system and hence leads to loss. The loss coefficient α_{NO}

https://doi.org/10.1017/S0022112010000133 Published online by Cambridge University Press

evaluated for short nozzles (nozzle length is small compared to acoustic wavelength) is given by (Zinn 1972)

$$\alpha_{NO} = -\left[M_N\left(\frac{\gamma+1}{2}\right)\left(1+\frac{\gamma+1}{2}M_N^2\right)\right], \quad M_N = \frac{\bar{m}l}{\bar{\rho}a}, \tag{12}$$

where M_N is the Mach number at the nozzle entrance plane. Even though a closed–closed boundary condition is assumed for the rocket combustion chamber, some part of the acoustic energy is carried away by the mean flow, the effect of which has to be accounted for in the governing equations. It is a standard practice (Culick 2006) to use the natural duct modes as the basis for projecting the equations and at the same time include the effect of the nozzle as a damping term in the governing equation. An acoustic boundary layer develops because of the viscous effect and no-slip boundary condition at the propellant surface. The effect is modelled as a volumetric sink term with the damping coefficient ξ_m given by (Matveev 2003):

$$\xi_m = -\left(C_1\frac{\omega_m}{\omega_1} + C_2\sqrt{\frac{\omega_1}{\omega_m}}\right), \tag{13}$$

where ω_m is the frequency of the mth Galerkin mode, C_1 and C_2 are constants that determine ξ_m. For the rocket motor considered in table 1, $l = 8$ m (a medium-sized motor) and the frequency of oscillations encountered during the limit cycle oscillation is 66.25 Hz (see § 7.3), which is close to the fundamental mode of the rocket configuration. Hence, the frequency of oscillation is not very small and viscous damping is expected to play a role. The higher acoustic modes will have higher frequencies and are affected by viscous damping and hence viscous damping has to be included. Moreover, the viscous damping coefficients chosen for the present simulations are small ($C_1, C_2 \sim O(10^{-2})$) compared with the nozzle damping ($\alpha_{NO} \sim O(10^{-1})$). The decay of the mth Galerkin pressure mode due to damping is given by

$$\frac{\partial P_m}{\partial t} = (\xi_m + \alpha_{NO})P_m. \tag{14}$$

The right-hand side of (14) is added to the right-hand side of (11) to account for the losses. A similar analysis is performed by Matveev (2003). The final acoustic momentum and energy equations are as follows:

$$\dot{U}_n + 2\sum_{m=1}^{N}\left(U_m I^1_{n,m} + P_m I^2_{n,m} + R^c_m I^3_{n,m} + R^s_m I^4_{n,m}\right) = 2\left\{k_m N^1_n - M N^2_n - \gamma N^3_n\right\}, \tag{15}$$

$$\dot{P}_n - (\xi_n + \alpha_{NO})P_n + \frac{2}{\gamma M}\left(\sum_{m=1}^{N}\left[U_m I^5_{n,m} + P_m I^6_{n,m} + R^c_m I^7_{n,m}\right]\right) = \frac{2}{\gamma M}\left\{\gamma M^2 N^4_n - (\gamma M)^2 N^5_n\right\}. \tag{16}$$

3.4. *Unsteady burn rate*

The unsteady burning of the propellant in response to the acoustic oscillations is shown to be the main driving source of acoustic instabilities in SRMs (Williams 1962; Kuo & Summerfield 1984). Gusachenko & Zarko (2008) give an excellent review of the unsteady solid propellant burn rate models. The burn rate fluctuates in response to acoustic pressure and velocity (parallel to the propellant surface) oscillations in the chamber (Culick 1968). Much less is known about the velocity coupling models and only *ad hoc* response functions are used for the SRM stability

https://doi.org/10.1017/S0022112010000133 Published online by Cambridge University Press

analysis (Levine & Baum 1983; Baum & Levine 1986). The acoustic velocity leads to the convective heat transfer at the propellant surface leading to unsteady burn rates. Sometimes flow reversal takes place which further increases the nonlinearity of the response. In this paper, acoustic pressure–burn rate coupling alone is investigated, as the acoustic velocity–burn rate coupling needs a more involved treatment. The models available to study acoustic velocity–burn rate coupling are very few and are insufficient to represent the dynamics involved in sufficient detail.

On the other hand, a number of models exist for unsteady burn rate–acoustic pressure coupling. When a propellant burns, there exist a condensed phase and a gas phase above the propellant surface. The flame is present in the gas phase and most of the heat release is from that phase. There are three basic time scales involved in the problem: (i) the reaction time scale of the flame, (ii) the flow time scale in the gas and condensed phases, (iii) the conduction time scale in the solid phase. A homogeneous propellant is analysed in the present case, which results in a premixed flame in the gas phase (Williams 1985). Premixed flame reaction time scales are very small compared with the acoustic time scales of the chamber. Furthermore, assuming a quasi-steady gas phase and a small condensed phase (solid and pyrolysed gaseous propellant) leads to analysing the dynamic response only in the solid phase (Williams 1962; Krier *et al.* 1968). Later, the restriction of small condensed phase was relaxed (Romanov 1999). Thermal inertia in the gas phase has been studied by Kumar & Lakshmisha (2000). Culick & Isella (2000) incorporated the dynamics in the condensed and gas phases. Apart from these, the burn rate response with phase transitions in the condensed phase (Cozzi, Deluca & Novozhilov 1999), propellant heterogeneity (Cohen & Strand 1985) and some specific class of propellants (Ward, Son & Brewster 1998) have been investigated. An asymptotic analysis has also been used to obtain the burn rate response of the propellant (Margolis & Armstrong 1986, 1988). However, the above analysis is mathematically complex and analytical solutions are very much limited.

The unsteady burn rate model used in this paper is from Krier *et al.* (1968). The model used here is simple but it captures the essential physics of the problem. The time lag between the acoustic pressure and burn rate is due to the finite speed of thermal wave propagation in the solid phase and the time scale ($\tau_{th} = \alpha/\bar{R}^2$) associated is comparable with the chamber acoustic time scale ($\tau_a = l/a$). The ratio $F = \tau_a/\tau_{th}$ for the SRM parameters shown in table 1 equals 1.37. A differential equation in time for non-dimensional temperature (T) inside the propellant grain is derived from the energy equation. The propellant burn rate is then related to the surface temperature by a power law (Krier *et al.* 1968). The dynamical boundary condition is written, relating the acoustic pressure and heat transfer at the propellant surface. The derivation of the equation is given in Krier *et al.* (1968) and the final nonlinear equation is as follows.

At each x location,

$$\left.\begin{array}{l} \dfrac{\partial T}{\partial \tau} - (1+R)\dfrac{\partial T}{\partial y} - \dfrac{\partial^2 T}{\partial y^2} = 0, \quad 0 \leqslant y < \infty, \quad 0 \leqslant \tau < \infty, \\ R = T_S^{m_p} - 1, \quad T_S(\tau) = T(y=0,\tau), \quad \tau/t = (l\bar{R}^2)/(a\alpha) = F, \end{array}\right\} \tag{17}$$

$$\text{boundary condition (BC)}: \left.\frac{\partial T}{\partial y}\right|_{y=0} = -\frac{(1+p)^{2n}((1+p)^{n/m_p} - H)}{1+R} - H(1+R), \tag{18}$$

$$T(y \to \infty, \tau) = 0,$$

$$\text{initial condition (IC)}: \quad T(y,0) = T_{st}(y) + T_p^0(y), \tag{19}$$

https://doi.org/10.1017/S0022112010000133 Published online by Cambridge University Press

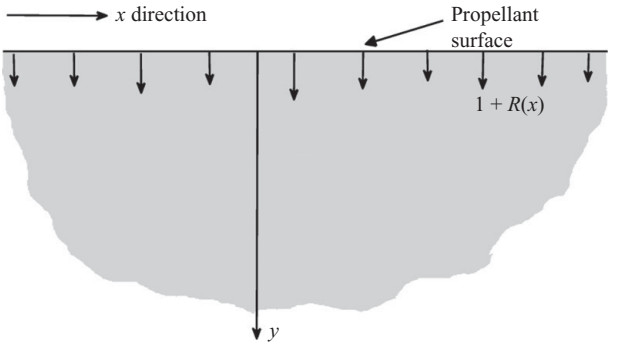


FIGURE 2. Geometry of the pressure-coupled propellant response model.

where $y = \tilde{y}/(\alpha/\bar{R})$, $\tau = t(l/a)/(\alpha/\bar{R}^2)$, $H = Q_S/(S_p(\tilde{T}_{S,0} - \tilde{T}_\infty))$, $T = (\tilde{T} - \tilde{T}_\infty)/(\tilde{T}_{S,0} - \tilde{T}_\infty)$, $T_{st} = \mathrm{e}^{-y}$, $\tilde{T}_\infty$ is the temperature of the propellant at $y \to \infty$, $\tilde{T}_{S,0}$ is the surface temperature of the propellant, T_{st} is the non-dimensional steady state temperature, T_p^0 is the non-dimensional temperature fluctuation at $t = 0$, n is the burn rate index, m_p is the pyrolysis coefficient, α is the thermal diffusivity of the propellant, Q_S is the overall heat release per unit mass at the propellant surface, S_p is the specific heat capacity of the propellant, y is the non-dimensional distance from the propellant surface, H is the ratio of the heat release at the propellant surface to its thermal capacity and F is the ratio of time scales of the chamber acoustics (τ_a) and transient heat conduction in the propellant (τ_{th}).

The coordinate system is fixed to the propellant surface which regresses according to the burn rate. The geometry is shown in figure 2. A Dirichlet-type boundary condition far from the propellant surface and a Neumann type at the surface (18), which comes from the balance between the amount of heat transfer from the flame in the gas phase to the propellant surface, are applied. The steady state temperature profile ($T_{st} = \mathrm{e}^{-y}$) obtained as the solution of the corresponding steady state problem $\partial T/\partial y + \partial^2 T/\partial y^2 = 0$, is exponentially decaying in y. The problem is formulated in one dimension as the response function predicted is shown to be accurate by Baum & Levine (1986) and Culick & Isella (2000). Note that $(1 + R)$ in (17) appears as a convection term, as the coordinate system is fixed to the propellant surface, which is regressing with the burn rate at that time (see figure 2). As described in § 3.1, this term contributes to the non-normality in the burn rate response. The other term in (17), i.e. the diffusion term, has no preferred direction associated with it ($(\mathrm{d}^2/\mathrm{d}x^2)^\dagger = \mathrm{d}^2/\mathrm{d}x^2$) and hence does not contribute to the non-normality of the burn rate response. The above advection–diffusion equation is shown to produce high transient growth by Reddy & Trefethen (1994). The presence of a non-normal behaviour in both combustion and acoustics leads to high transient growth when coupled together. Hence, the short-term dynamics obtained from both the unsteady burn rate and acoustic equations will be very different from those predicted by the classical linear stability theory for asymptotic time. It is now important to understand the various physical processes that contribute to the dynamics of the unsteady burn rate.

The mechanism of the burn rate–acoustic pressure coupling is as follows. The reaction rate of a premixed flame is dependent on the pressure and, to a weaker extent, on the temperature. During the compression part of the acoustic cycle, the flame speed increases, and the flame comes closer to the solid thereby causing more heat transfer to the solid. The pyrolysis of the propellant is assumed to obey the

https://doi.org/10.1017/S0022112010000133 Published online by Cambridge University Press

Arrhenius law, which under practical values of activation energy leads to a power-law dependence on surface temperature (Krier *et al.* 1968). Higher heat transfer to the solid phase increases the solid phase surface temperature and hence the burn rate. Thus, the acoustic forcing comes through the boundary condition stated in (18), which is a crucial difference from the earlier analysis of Balasubramanian & Sujith (2008*a*), where the forcing explicitly appears through the convective term in the equation.

From the physics of the problem, the temperature fluctuations are expected to be high near the propellant surface and decrease towards the chamber casing (Dirichlet boundary condition). Thus, it is necessary to cluster more grid points near the surface, which will yield accurate results with fewer grid points and hence less computational time (Anderson 1996). The transformation $\eta = e^{-ky}$ is used; k controls the amount of grid clustered near the propellant surface.

Equation (17) with boundary (18) and initial (19) conditions is transformed into

$$\left.\begin{gathered} \frac{\partial T}{\partial \tau} + ((1+R)k\eta - k^2\eta)\frac{\partial T}{\partial \eta} - (k\eta)^2\frac{\partial^2 T}{\partial \eta^2} = 0, \quad 0 \leqslant \eta \leqslant 1, \quad 0 \leqslant \tau \leqslant \infty, \\ R = T_S^{m_p} - 1, \quad T_S(\tau) = T(\eta = 1, \tau), \\ \text{BC}: \left.\frac{\partial T}{\partial \eta}\right|_{\eta=1} = \frac{1}{k}\left(\frac{(1+p)^{2n}((1+p)^{n/m_p} - H)}{(1+R)} - H(1+R)\right), \quad T(\eta \to 0, \tau) = 0, \\ \text{IC}: \; T(\eta, 0) = \eta^{1/k} + T_p(\eta). \end{gathered}\right\} \tag{20}$$

Equation (20) is solved by a semi-implicit backward time central space (BTCS) scheme similar to that used by Junye (2000). The burn rate $R(x)$ at each axial location is obtained for the corresponding pressure at that location. Now, in order to use the source terms $R(x)$ in (15) and (16), $R(x)$ is projected onto the Galerkin modes and R_m^c, R_m^s are obtained as

$$\left.\begin{aligned} R_m^c(t) &= 2\int_0^1 R(x,t)\cos(\omega_m x)\,\mathrm{d}x, \\ R_m^s(t) &= 2\int_0^1 R(x,t)\sin(\omega_m x)\,\mathrm{d}x. \end{aligned}\right\} \tag{21}$$

To track the evolution of the system, the nonlinear equations (15) and (16) are integrated using the fourth-order Runge–Kutta (RK4) method with (20) updated at each sub-step of RK4 using the semi-implicit BTCS scheme. General conclusions about non-normality of the system can be made with the linearized equations. To quantify the effect of non-normality, the equations are cast in a standard linearized form, which can be analysed using an existing framework (Schmid & Henningson 2001).

4. Short-term dynamics and transient growth

To analyse the non-normal system, a state space vector formulation is used. Farrell & Ioannou (1996) developed a generalized stability theory for non-normal linear operators, in the context of atmospheric sciences. In the state space vector representations, a general N dimensional linear dynamical system is given by

$$\frac{\mathrm{d}\chi(t)}{\mathrm{d}t} = L\chi(t), \tag{22}$$

where L is an N dimensional square matrix. Balasubramanian & Sujith (2008*a*, 2008*b*) have shown that L is non-normal ($LL^\dagger \neq L^\dagger L$) for a thermoacoustic system. The general solution is given by $\chi(t) = e^{Lt}\chi(0)$, where $\chi(0)$ is the initial

https://doi.org/10.1017/S0022112010000133 Published online by Cambridge University Press

condition. An amplification factor is defined as $\sigma^2 = \langle\chi(t)|\chi(t)\rangle / \langle\chi(0)|\chi(0)\rangle$ ($\langle\bullet|\bullet\rangle$ denotes inner product in the linear vector space, $|\chi(t)\rangle = \chi(t)$, $\langle\chi(t)| = \chi^{\dagger}(t)$) as a measure of growth or decay of fluctuations in the system during its time evolution. Note that σ^2 can be related to some physical quantity such as the disturbance energy of the system (Schmid & Henningson 2001; Nagaraja, Kedia & Sujith 2009). Moreover, σ^2 will depend on the choice of the initial condition. The maximum value of σ^2 for all possible initial conditions is given by $G(t) = \mathrm{Max}_{\chi(0)}\left(\langle\chi(t)|\chi(t)\rangle / \langle\chi(0)|\chi(0)\rangle\right) = \|\mathrm{e}^{Lt}\|^2$ (Golub & Van Loan 1989). Here, $\|A\|$ denotes the 2-norm of the matrix A. The optimum initial condition (V_{opt}) to attain the maximum transient growth is the first column of the matrix V, given by the singular value decomposition of $\mathrm{e}^{Lt} = UDV^{\dagger}$ (Golub & Van Loan 1989; Nagaraja *et al.* 2009), where D is a diagonal matrix with entries as singular values arranged in descending order. Now, from the evolution of $G(t)$, maximum amplification over all possible initial conditions and time can be obtained. For a system that is unstable according to the classical linear stability theory, $G_{max} = \max(G(t)) \to \infty$. For a system that is stable according to the classical linear stability and is highly non-normal, $G_{max} \gg 1$. This shows high initial transient growth. For a linearly stable normal system, $G_{max} = 1$.

5. Linear analysis

To analyse the generalized stability of the system as discussed in the previous section, (15), (16) and (20) are linearized to give the following:

$$\dot{U}_n + 2\sum_{m=1}^{N}\left(U_m I^1_{n,m} + P_m I^2_{n,m} + R^c_m I^3_{n,m} + R^s_m I^4_{n,m}\right) = 0, \tag{23}$$

$$\dot{P}_n - (\xi_n + \alpha_{NO})P_n + \frac{2}{\gamma M}\left(\sum_{m=1}^{N}\left[U_m I^5_{n,m} + P_m I^6_{n,m} + R^c_m I^7_{n,m}\right]\right) = 0, \tag{24}$$

$$\left.\begin{aligned} &\frac{\partial T_p}{\partial \tau} + (k - k^2\eta)\frac{\partial T_p}{\partial \eta} - (k\eta)^2\frac{\partial^2 T_p}{\partial \eta^2} + m_p\eta^{1/k}T_{ps} = 0, \\ &R = m_p T_{ps}, \quad T_{ps}(t) = T_p(\eta = 1, t), \qquad \tau/t = l\bar{R}^2/a\alpha = F, \\ &\mathrm{BC}: \quad \left.\frac{\partial T_p}{\partial \eta}\right|_{\eta=1} = \left(\frac{AT_{ps} - Bp}{k}\right), \qquad T_p(\eta \to 0, \tau) = 0, \end{aligned}\right\} \tag{25}$$

where $A = (2H-1)/m_p$, $B = (2H-1/m_p-2)/n$, T_p is the fluctuating temperature in the propellant given by $T_p = T - T_{st} = T - \eta^1/k$. Equation (25) has to be applied at all axial locations. Because R is a linear function of T_{ps}, T_p can be decomposed as follows:

$$T_p(x,t) = \sum_{k=1}^{N}\left[T^c_k(t)\cos(\omega_k x) + T^s_k(t)\sin(\omega_k x)\right], \quad R^c_k = T^c_k/m_p, \quad R^s_k = T^s_k/m_p. \tag{26}$$

The above expression, when substituted in (25) and then projected onto the Galerkin basis as described earlier, leads to the following equations:

$$\left.\begin{aligned} &\frac{\partial T^c_n}{\partial \tau} + (k - k^2\eta)\frac{\partial T^c_n}{\partial \eta} - (k\eta)^2\frac{\partial^2 T^c_n}{\partial \eta^2} + m_p\eta^{1/k}T^c_{sn} = 0 \\ &T^c_{sn}(t) = T^c_n(\eta = 1, t), \\ &\mathrm{BC}: \quad \left.\frac{\partial T^c_n}{\partial \eta}\right|_{\eta=1} = \left(\frac{AT^c_{sn} - B\gamma M P_n}{k}\right), \quad T^c_n(\eta \to 0, \tau) = 0, \end{aligned}\right\} \tag{27}$$

https://doi.org/10.1017/S0022112010000133 Published online by Cambridge University Press

$$\left.\begin{aligned} &\frac{\partial T_n^s}{\partial \tau} + (k - k^2\eta)\frac{\partial T_n^s}{\partial \eta} - (k\eta)^2\frac{\partial^2 T_n^s}{\partial \eta^2} + m_p \eta^{1/k} T_{sn}^s = 0, \\ &T_{sn}^s(t) = T_n^s(\eta = 1, t), \\ &\text{BC}: \quad \left.\frac{\partial T_n^s}{\partial \eta}\right|_{\eta=1} = \left(\frac{A T_{sn}^s}{k}\right), \quad T_n^s(\eta \to 0, \tau) = 0. \end{aligned}\right\} \tag{28}$$

An important observation in the linear regime is that the Galerkin pressure mode is absent in the boundary condition for (28). Hence, R_n^s is not affected (in the linearized equations) by the acoustic fluctuations, and it evolves depending only on its initial condition. However, it affects the acoustic momentum equation (23) through the $R_m^s I_{n,m}^4$ term. Equations (23), (24), (27) and (28) can be cast in the form of (22). Equations (27) and (28) are discretized using a second-order central difference at M_g equally spaced points in 'η'. The linearized equations are

$$\left.\begin{aligned} \frac{\mathrm{d}\chi}{\mathrm{d}t} &= L\chi, \\ \chi &= \left(\Omega \;\; \Psi_1^c \;\; \Psi_2^c \;\; .. \;\; \Psi_N^c \;\; \Psi_1^s \;\; \Psi_2^s \;\; \ldots \;\; \Psi_N^s\right)_{1\times 2NM_g}, \\ \Omega &= (U_1 P_1 \;\; \ldots \;\; U_N P_N)_{1\times 2N}^{\mathrm{T}}, \quad \mathrm{T} \text{ represents matrix transpose}, \\ \Psi_n^c &= \left(\beta_1 T_{n(1)}^c \beta_2 T_{n(2)}^c \;\; \ldots . \;\; \beta_{M_g-1} T_{n(M_g-1)}^c\right)_{1\times(M_g-1)}^{\mathrm{T}}, \\ \Psi_n^s &= \left(\beta_1 T_{n(1)}^s \beta_2 T_{n(2)}^s \;\; \ldots . \;\; \beta_{M_g-1} T_{n(M_g-1)}^s\right)_{1\times(M_g-1)}^{\mathrm{T}}, \end{aligned}\right\} \tag{29}$$

where the subscripts $n(1), n(2), n(3), \ldots, n(M_g - 1)$ represent the fluctuating temperature at 1st, 2nd, 3rd, ..., $(M_g - 1)$th points from the propellant surface for the nth mode. The homogeneous boundary condition $(T_n^c(\eta \to 0, \tau) = T_n^s(\eta \to 0, \tau) = 0)$ at the last point leaves Ψ_n^c and Ψ_n^s with $(M_g - 1)$ discrete points. The linear operator matrix is expanded in Appendix B. Now, as mentioned in § 2, (25) indicates the extra degree of freedom for the system apart from acoustics and it appears as extra variables Ψ_n^c, Ψ_n^s in (29). This implies that not only does the system comprises acoustic variables but it is also an extended one with variables from the burn rate response. Hence, acoustic energy (Rienstra & Hirschberg 2008), which defines the growth or decay of acoustic oscillations, is inadequate. A new generalized disturbance energy is defined which accounts for the perturbations in burn rate variables (Ψ_n^c, Ψ_n^s). A formal derivation of fluctuating thermal energy in the propellant is performed. The thermal energy obtained is then added to the acoustic energy with appropriate weight factors (arrived at from the consideration of entropy generation at the propellant surface) to get the 'generalized disturbance energy'. The factor β_i in (29) is present for the reason, that the 2-norm or L2 norm of $\chi(t)$ represents the disturbance energy. The following section deals with the disturbance energy and its relation to $\langle \chi(t) | \chi(t) \rangle$.

6. Generalized disturbance energy

As mentioned in § 4, σ^2, which is a relative measure of the 2-norm of $\chi(t)$ $(\|\chi(t)\| = (\langle \chi(t) | \chi(t) \rangle)^{1/2})$, can be related to the energy in the disturbance calculated from the state space variables in (29). From our analysis, this energy has two components. The first component is from the chamber acoustic field and the second is from the unsteady thermal energy of the propellant. Energy in the acoustic field can be characterized by the familiar acoustic energy $\tilde{E}_{ac}(t) = \frac{1}{2}\iiint_{chamber\ volume} [(\bar{\rho}\tilde{u}'(x,t))^2 + (\tilde{p}'(x,t)/\bar{\rho}a^2)^2]\,\mathrm{d}V$ (Rienstra & Hirschberg 2008).

https://doi.org/10.1017/S0022112010000133 Published online by Cambridge University Press

Non-dimensionalizing the above by $\bar{\rho}u_m^2 S_c l/2$ leads to the following:

$$E_{ac}(t) = \frac{\tilde{E}_{ac}(t)}{\frac{1}{2}\bar{\rho}u_m^2 S_c l} = \int_0^1 \left[(u(x,t))^2 + \left(\frac{p(x,t)}{\gamma M}\right)^2\right] = \frac{1}{2}\sum_{n=1}^{N}\left(U_n^2 + P_n^2\right). \tag{30}$$

Now a similar expression for the fluctuating energy stored in the solid phase of the propellant has to be calculated to get the total disturbance energy. Equation (17) is written in its linearized and dimensional form for the fluctuating temperature $\tilde{T}'$ as

$$\rho_p S_p\left(\frac{\partial \tilde{T}'}{\partial \tilde{t}} - \bar{R}\frac{\partial \tilde{T}'}{\partial \tilde{y}} - \tilde{R}'\frac{\partial \tilde{T}_{st}}{\partial \tilde{y}}\right) = \lambda_p \frac{\partial^2 \tilde{T}'}{\partial \tilde{y}^2}, \tag{31}$$

where λ_p is the thermal conductivity of the solid phase of the propellant. Multiplying the above equation by $\tilde{T}'/\bar{T}$ and rearranging, we obtain

$$\frac{\rho_p S_p}{2\bar{T}}\frac{\partial \tilde{T}'^2}{\partial \tilde{t}} = \frac{\lambda_p}{\bar{T}}\left(\frac{\partial}{\partial \tilde{y}}\left(\tilde{T}'\frac{\partial \tilde{T}'}{\partial \tilde{y}}\right) - \left(\frac{\partial \tilde{T}'}{\partial \tilde{y}}\right)^2\right) + \frac{\rho_p S_p \bar{R}}{2\bar{T}}\frac{\partial \tilde{T}'^2}{\partial \tilde{y}} + \frac{\rho_p S_p}{2\bar{T}}\frac{\partial \tilde{T}_{st}}{\partial \tilde{y}}\tilde{R}'\tilde{T}'. \tag{32}$$

Integrating (32) over the entire solid phase propellant volume and applying Gauss divergence theorem, we get

$$\begin{aligned}\frac{\rho_p S_p}{2\bar{T}}\frac{\partial \iiint_{V_1} \tilde{T}'^2 \,\mathrm{d}V}{\partial \tilde{t}} &= \frac{1}{\bar{T}}\left(\int\int_{S_l} \lambda_p \tilde{T}'\frac{\partial \tilde{T}'}{\partial \tilde{y}}\,\mathrm{d}S + \frac{\rho_p S_p \bar{R}}{2}\left(\tilde{T}'^2|_{S_u} - \tilde{T}'^2|_{S_l}\right)\right) \\ &\quad + \frac{\rho_p S_p}{2\bar{T}}\iiint_{V_1}\frac{\partial \tilde{T}_{st}}{\partial \tilde{y}}\tilde{R}'\tilde{T}'\,\mathrm{d}V - \frac{\lambda_p}{\bar{T}}\iiint_{V_1}\left(\frac{\partial \tilde{T}'}{\partial \tilde{y}}\right)^2 \mathrm{d}V,\end{aligned} \tag{33}$$

where V_1 is the entire propellant volume, S_l is the entire propellant surface, S_u is propellant upper surface and S_l is the propellant lower surface (casing). The left-hand side of (33) is a positive definite quantity, which is the fluctuating energy due to temperature fluctuations in the propellant. The first term in the right-hand side is the corresponding energy flux term. The second term is due to the contributions from the unsteady burn rate and the last term is from the loss due to thermal conduction (the term is always negative). Now the equation is the conservation equation for the fluctuating energy $\tilde{E}_p$ present in the solid propellant. The fluctuating energy $\tilde{E}_p$ is

$$\tilde{E}_p = \frac{\rho_p S_p}{2\bar{T}}\iiint_{V_1}\tilde{T}'^2\,\mathrm{d}V = \frac{\rho_p S_p}{2\bar{T}}(\tilde{T}_{S,0} - \tilde{T}_\infty)^2 l S_l \frac{\alpha}{\bar{R}}\int_{y=0}^{\infty}\int_{x=0}^{1} T_p^2\,\mathrm{d}x\,\mathrm{d}y. \tag{34}$$

Non-dimensionalizing the above by $\bar{\rho}u_m^2 S_c l/2$, substituting for T_p from (26) and substituting $\eta = \mathrm{e}^{-ky}$, we obtain

$$E_p = \frac{\tilde{E}_p}{\frac{1}{2}\bar{\rho}u_m^2 S_c l} = \frac{\delta}{2}\int_{\eta=0}^{1}\sum_{n=1}^{N}\left(\left(\frac{T_n^c}{\sqrt{\eta}}\right)^2 + \left(\frac{T_n^s}{\sqrt{\eta}}\right)^2\right)\mathrm{d}\eta, \tag{35}$$

where $\delta = (\rho_p S_p \alpha S_l(\tilde{T}_{S,0} - \tilde{T}_\infty)^2)/(\bar{R}\bar{\rho}\bar{T}u_m^2 S_c k)$. Discretizing in the η domain leaves (35) as

$$E_p = \frac{\tilde{E}_p}{\frac{1}{2}\bar{\rho}u_m^2 S_c l} = \frac{\delta}{2}\sum_{n=1}^{N}\sum_{i=1}^{M_g-1}\left(\left(\frac{T_n^c}{\sqrt{\eta_i}}\right)^2 + \left(\frac{T_n^s}{\sqrt{\eta_i}}\right)^2\right)\Delta\eta. \tag{36}$$

Now, the weightage to energies $\tilde{E}_{ac}$ and $\tilde{E}_p$ in forming the total disturbance energy $\tilde{E}_T$ is fixed by considering the energy from entropy fluctuations. Chu (1965) has

https://doi.org/10.1017/S0022112010000133 Published online by Cambridge University Press

derived an expression for the disturbance energy ($\tilde{E}_{chu}$) and is given by $\tilde{E}_{chu}(t) = (1/2)\iiint_{chamber\ volume}[(\bar{\rho}\tilde{u}'(x,t))^2 + (\tilde{p}'(x,t)/(\bar{\rho}a^2))^2 + ((\gamma-1)\bar{P})/\gamma(\tilde{s}'/\Re)^2]\,\mathrm{d}V$, where $\tilde{s}'$ is the entropy fluctuation and $\Re$ is the characteristic gas constant of the gas in the combustion chamber. Flame is the source of entropy fluctuations in the motor. The entropy fluctuations are computed from propellant surface temperature and acoustic fluctuations, as derived by Krier *et al.* (1968), as

$$\frac{\tilde{s}'}{\Re} = \frac{\gamma}{\gamma-1}\Theta\left[\left(2nH - 2n - \frac{n}{m_p} - 1\right)p + (2m_p + 1 - 2m_pH)T_{ps}\right], \tag{37}$$

where $\Theta = (\tilde{T}_{S,0} - \tilde{T}_\infty)/(\tilde{T}_f)$. Note that $\tilde{T}_f$ is the steady flame temperature. Now the coefficient proportional to T_{ps}^2 in the entropy part of $\tilde{E}_{chu}$ after substituting (37) in $\tilde{E}_{chu}$ is $[\Theta(2m_p + 1 - 2m_pH)]^2(\gamma P)/(\gamma - 1)$. This gives the weight factor W_f for $\tilde{E}_p$ which has to be added to $\tilde{E}_{ac}$. Hence, the total disturbance energy is

$$\tilde{E}_T = \tilde{E}_{ac} + W_f\tilde{E}_p,\ W_f = \frac{2\gamma\bar{P}\bar{T}}{(\gamma-1)\rho_pS_p}\left[\frac{\Theta(2m_p + 1 - 2m_pH)}{\tilde{T}_{S,0} - \tilde{T}_\infty}\right]^2. \tag{38}$$

Non-dimensionalizing as before, we get the total non-dimensional generalized disturbance energy E_T. This energy incorporates the contributions from the entropy fluctuations released by the flame as well as the temperature fluctuations inside the propellant:

$$E_T = \frac{\tilde{E}_T}{\frac{1}{2}\bar{\rho}u_m^2S_cl} = E_{ac} + W_fE_p. \tag{39}$$

Now, using (30) and (36), we get

$$\begin{aligned} E_T(t) &= \frac{\tilde{E}_T}{\frac{1}{2}\bar{\rho}u_m^2S_cl} = E_{ac} + W_fE_p \\ &= \frac{1}{2}\sum_{n=1}^{N}\left[\left(U_n^2 + P_n^2\right) + \sum_{i=1}^{M_g-1}\left(\left(\beta_iT_n^c\right)^2 + \left(\beta_iT_n^s\right)^2\right)\right] = \frac{1}{2}\|\chi(t)\|^2 \end{aligned} \tag{40}$$

where $\beta_i = \sqrt{\Delta\eta\delta W_f/\eta_i}$. Thus, the 2-norm of $\chi(t)$ is related to the physical generalized disturbance energy and σ^2 gives the amplification of the same during the system evolution. It should be noted that Chu's energy is derived in the limit of zero mean flow Mach number. However, in the present case, the mean flow Mach number is not zero ($M \sim 0.1$). If one includes the energy contribution due to mean flow, the disturbance energy (E_T) cannot be represented by the L2 norm. The reason for choosing E_T as the L2 norm is as follows. In a dynamical system, L2 norm can be calculated easily using singular value decomposition (SVD). The optimum initial condition and the maximum transient growth can then be obtained directly from the SVD. The choice of norms other than the L2 norm brings the complication of defining new inner products. The inner products thus defined can be mathematically inconsistent, and some special techniques (such as adjoint optimization) other than SVD should be used, which is beyond the scope of this paper. Hence, in this analysis, Chu's energy is used, so that E_T coincides with the L2 norm. The L2 norm can then be computed using SVD.

https://doi.org/10.1017/S0022112010000133 Published online by Cambridge University Press

Gas properties	Propellant properties	Rocket combustion chamber dimension
$\bar{p} = 60$ bar	$\Delta h = 7$ MJ kg^{-1}	$l = 8$ m
$\bar{T} = 2900$ K	$\alpha = 1.6\times10^{-6}$ m^2 s^{-1}	$S_l = 1.59$ m
$\bar{\rho} = 4.82$ kg m^{-3}	$m_p = 6$	$S_c = 0.2$ m^2
$\gamma = 1.35$	$n = 0.4$	Numerical parameters
$\Re = 287$ J kg^{-1} K^{-1}	$\bar{R} = 0.017$ m s^{-1}	$N = 5$
$H = 0.76$	$\rho_p = 1800$ kg m^{-3}	$M_g = 150$
$\Theta = 0.19$	$S_p = 3542$ J kg K^{-1}	Time step $\Delta t = 0.005$

TABLE 1. SRM parameter values and operating conditions.

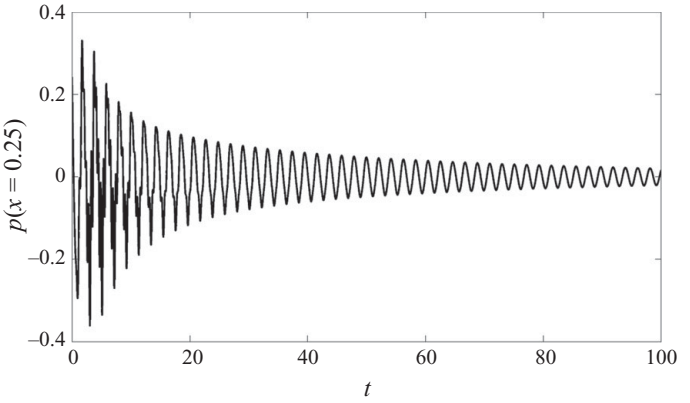


FIGURE 3. The evolution of acoustic pressure at $x = 0.25$ for a linearly stable system. $U_1(0) = 3$, $P_1(0) = 3$, $P_{m\neq1}(0) = U_{m\neq1}(0) = 0$, $MT_p(\eta, 0) = 0$, $C_1 = 0.05$, $C_2 = 0.001$.

7. Results and discussion

Simulations are performed for a rocket motor, whose system parameters are given in table 1. The numerical simulations are performed with the simulation parameters N, M_g and time-integration time step Δt as shown in table 1. Increasing N, M_g and decreasing Δt beyond the above values leads to a difference of less than 1 %. Hence, the above values are chosen for all simulations shown below. The damping coefficients C_1 and C_2 are varied to get a different dynamical behaviour for the simulation.

7.1. *Linearly stable and unstable system*

The linearized equation (22) is analysed for the stability of the system to small-amplitude disturbances. Eigenvalues of the discretized linear operator L determine the linear stability of the system in the asymptotic time limit. If all the eigenvalues lie in the left half of the complex plane, the system is asymptotically stable to small disturbances. This is called 'classical linear stability'. However, the short-term behaviour is different due to the non-normal nature of the linearized operator. Using Farrell & Ioannou's (1996) terminology, a system with $G_{max} = 1$ is called 'linearly stable' (generalized linear stability) and the finite amplitude small disturbances die down monotonically. The time evolution of unsteady oscillations is shown at one-fourth of the motor length ($l/4$) from the head end as a representative position. Acoustic pressure oscillation is shown in figure 3 for a system, stable according to the classical linear stability. The amplitude decays in the asymptotic time limit, eventually reaching a stable fixed point. The phase space plot between $p(x = 1/4)$ and

https://doi.org/10.1017/S0022112010000133 Published online by Cambridge University Press

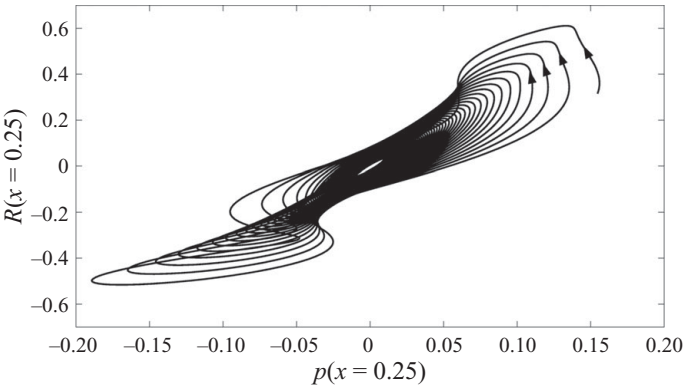


FIGURE 4. The phase portrait of the acoustic pressure and the unsteady burn rate at $x = 0.25$. $U_1(0) = 3$, $P_1(0) = 3$, $P_{m\neq1}(0) = U_{m\neq1}(0) = 0$, $MT_p(\eta, 0) = 0$, $C_1 = 0.05$, $C_2 = 0.001$.

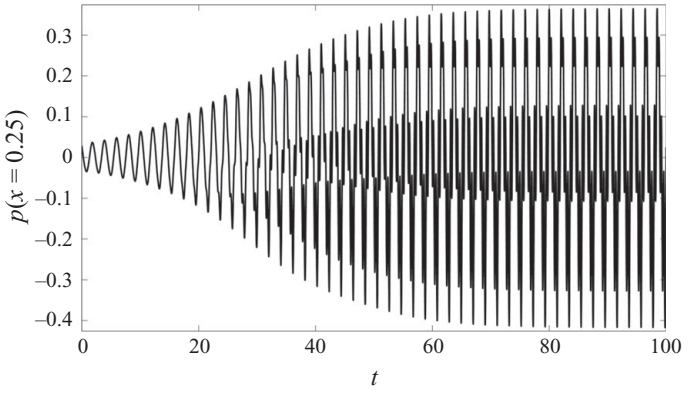


FIGURE 5. The evolution of acoustic pressure at $x = 0.25$ for a linearly unstable system. $U_1(0) = 0.3$, $P_1(0) = 0.3$, $P_{m\neq1}(0) = U_{m\neq1}(0) = 0$, $MT_p(\eta, 0) = 0$, $C_1 = 3 \times 10^{-4}$, $C_2 = 1 \times 10^{-4}$.

$R(x = 1/4)$ (figure 4) shows a spiral trajectory, eventually collapsing to a single point (0, 0) corresponding to the steady flow (arrows indicate the direction of the time evolution). This type of fixed point is called 'stable focus'. The actual dimensions of the phase space in the modal and discretized form is $2N + 2N(M_g - 1) = 2N(M_g)$, which corresponds to the total number of state space variable in (29). The plot in figure 4 is just the projection of $2N(M_g)$ space onto a two dimensional space. Hence, we observe apparent intersections of the phase trajectories, which are actually evolving without intersection in a higher dimension space. On the other hand, if the real part of one of the eigenvalues is positive, the system is linearly unstable. Figure 5 shows the acoustic pressure evolution from a small initial disturbance for a linearly unstable system. Initially, the oscillations grow exponentially as predicted by linear stability theory, reaching amplitudes where nonlinear terms start dominating. The nonlinear terms in (15) and (16) start dominating, balancing the driving terms resulting in the formation of oscillations of constant amplitude called a limit cycle. The corresponding phase plot between $p(x = 1/4)$ and $R(x = 1/4)$ after removing the transients leaves a closed curve (figure 6). This corresponds to limit cycles, where the trajectories close itself as $t \to \infty$. The presence of apparent multiple intersections in figure 6 shows the presence of more dominant frequencies, which is a characteristic

https://doi.org/10.1017/S0022112010000133 Published online by Cambridge University Press

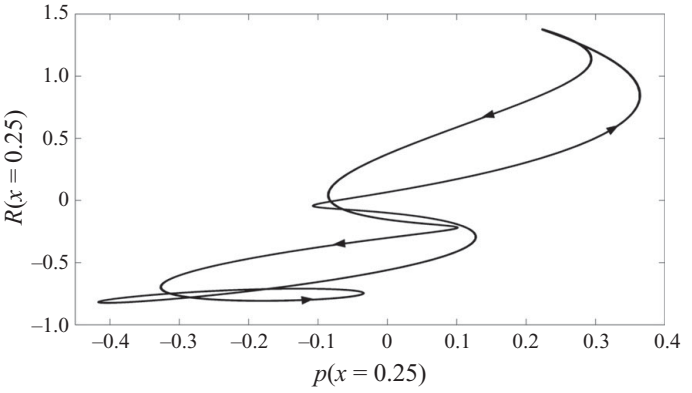


FIGURE 6. The phase portrait of the acoustic pressure and unsteady burn rate at $x = 0.25$. $U_1(0) = 0.3$, $P_1(0) = 0.3$, $P_{m\neq1}(0) = U_{m\neq1}(0) = 0$, $MT_p(\eta, 0) = 0$, $C_1 = 3 \times 10^{-4}$, $C_2 = 1 \times 10^{-4}$.

of limit cycle oscillations in SRMs. The existence of a limit cycle was explained by Culick (1976*a*) with second-order nonlinear acoustics. However, another important phenomenon is the occurrence of 'pulsed instabilities' (Blomshield *et al.* 1997*b*) in SRMs. This is a type of instability leading to unpredicted damage of the motors and has not been explained to date with a physics-based acoustic–burn rate coupling model. This issue is addressed in § 7.3. Before examining the nonlinear regime of oscillations, it is important to discuss some more interesting results pertaining to the non-normal nature of the linear operator L in the following section.

7.2. *Pseudospectra and transient growth*

The linear operator (29) in its discretized form (L matrix) is used for pseudospectra computation. For normal operators, resonance (maximum amplification) happens at the eigenvalues; at other points, the amplification is inversely proportional to the distance of the forcing frequency from the nearest eigenvalue. However, for non-normal operators, resonant amplification of many orders occurs far from the eigenvalues and is called 'pseudoresonance' (Trefethen & Embree 2005). The ε pseudospectra plot is used to analyse non-normal operators and z is called an ε pseudoeigenvalue of the operator L, if it satisfies $\|(zI - L)^{-1}\| \geqslant \varepsilon^{-1}$ (Trefethen & Embree 2005). The perturbations ε given are very small compared with the size of the linear operator ($\varepsilon \ll \|L\|$). For normal operators, ε pseudospectrum consists of concentric circles, confirming the inversely proportional relationship between the amplification and the distance between the excitation frequency and the nearest eigenfrequency of the system. However, for non-normal operators the contours are distorted.

Figure 7(*a*) shows that the pseudospectra of the L matrix are highly distorted near the imaginary axis. The system considered is stable according to the classical linear stability theory. All the eigenvalues of the system lie on the left half of the complex plane. The perturbation in the linear operator L is depicted in its pseudospectra. The relation between transient growth and the geometry of the pseudospectra is described by Trefethen & Embree (2005). The contours spill over to the right half of the complex plane, which is an indication of transient growth in the system evolution. The zoomed-in contour of figure 7(*a*) near the origin is shown in figure 7(*b*). For example, a perturbation of $\varepsilon = 10^1$ ($\varepsilon/\|L\| = 5.33 \times 10^{-4}$) leads to the spilling of the pseudospectra to the right by $z = 72$ units from the imaginary axis. From this, the transient growth is estimated to be $(z/\varepsilon)^2 = 7.2^2 = 51.84$ (Trefethen & Embree 2005).

https://doi.org/10.1017/S0022112010000133 Published online by Cambridge University Press

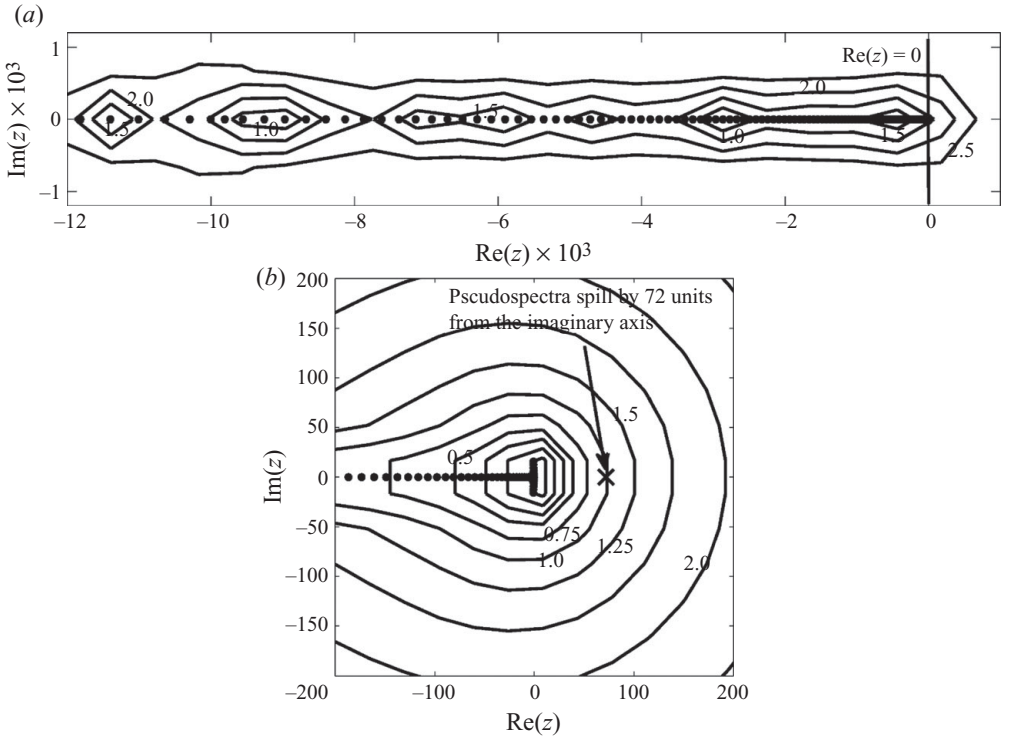


FIGURE 7. (*a*) Pseudospectra of the non-normal linear operator *L*. (*b*) Zoomed-in view near the origin and the calculation of the lower bound for the maximum transient growth. The contour value represents $\log_{10}\varepsilon$. $C_1 = 0.03$, $C_2 = 0.02$, $\|L\| = 1.88 \times 10^4$, $\varepsilon_{max} = 1 \times 10^{2.5}$, $\varepsilon_{max}/\|L\| \ll 1$.

This is just one point in the ε contour. Maximizing this over all ε contours results in 'Kreiss constant (κ)', which gives the lower bound for the maximum transient growth (G_{max}). For a normal system, ε contours move proportionally outwards with z and hence $\kappa = 1$ with no transient growth. Thus, qualitative information can be obtained from the contours of the pseudospectra. As is shown in § 6 the square of the 2-norm of the state space vector equals the total disturbance energy in the system. Hence, the transient growth obtained now directly gives the disturbance energy amplification. We also note that a very small perturbation (0.1 %) leads to an energy rise of 2 orders of magnitude. All these are obtained from investigating the geometry of the pseudospectra.

The exact calculation of maximum transient growth is to evolve $G(t) = \|\exp(Lt)\|^2$ and find its maximum as discussed in § 4. Figure 8(*a*) shows the evolution of $\|e^{Lt}\|$ and the maximum transient growth is found to be $128.9^2 = 1.66 \times 10^4$, which is higher than the previous estimate based on the lower bound of G_{max} from pseudospectra. Also, the same figure shows that the use of response function for modelling the acoustic–burn rate coupling gives rise to very small transient growth. The response function is calculated as follows. The unsteady burn rate equation (20) is solved for a forced pressure oscillation $p = p_0 \sin(\omega t)$ to get the unsteady burn rate in the form $R = R_0 \sin(\omega t + \phi)$. Here R_0 is obtained from the Fourier transform of the signal R at the frequency $\omega/2\pi$ and the phase from

https://doi.org/10.1017/S0022112010000133 Published online by Cambridge University Press

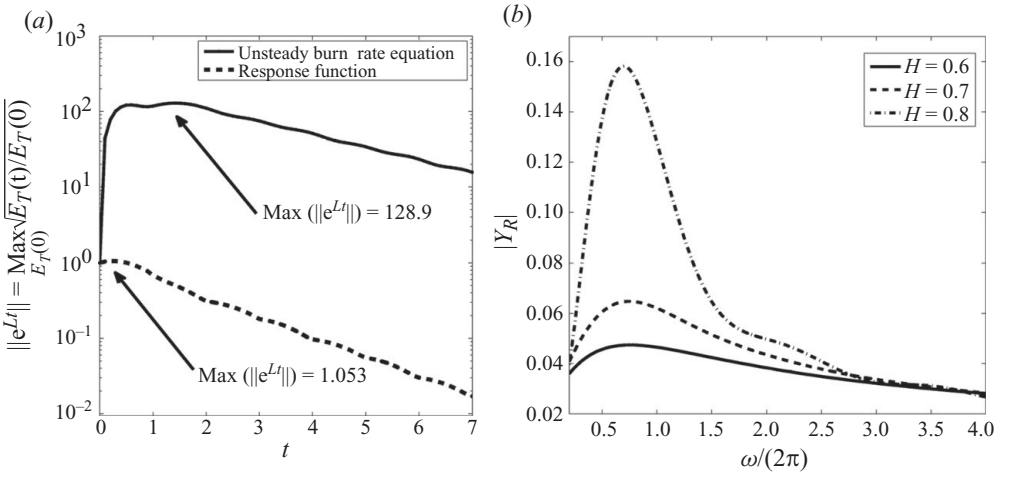


FIGURE 8. (*a*) Comparison of the evolution of $\|e^{Lt}\|$ with differential equation for unsteady burn rate and response function (Y_R) calculations, $C_1 = 0.03$, $C_2 = 0.02$, $\chi(0) = V_{opt}$. (*b*) The magnitude of the response functions ($|Y_R|$) of the propellant for various values of H.

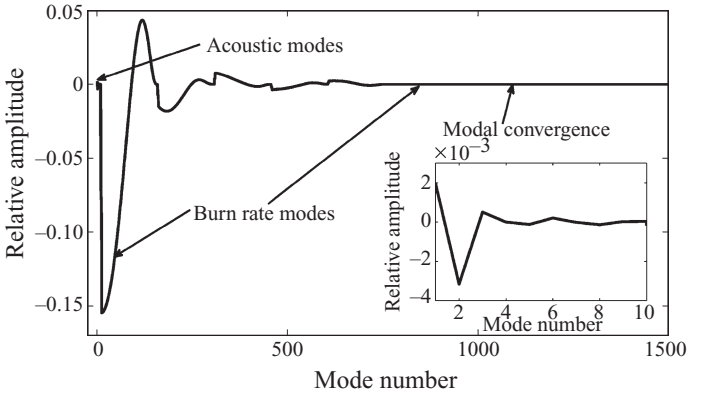


FIGURE 9. Relative amplitude of the optimum initial condition direction. Inset shows the relative amplitude of the acoustic modes, $C_1 = 0.03$, $C_2 = 0.02$, $\chi(0) = V_{opt}$, $N = 5$, $M_g = 150$.

$\cos\phi = \int_0^\infty p(t)R(t)\,\mathrm{d}t / (\sqrt{\int_0^\infty p^2(t)\,\mathrm{d}t}\sqrt{\int_0^\infty R^2(t)\,\mathrm{d}t})$. The response function (Y_R) used is $Y_R = R/p = R_0 e^{i\phi}/p_0$. The magnitude of Y_R for various excitation frequencies is shown in figure 8(*b*). It is also observed that the magnitude of Y_R is maximum around 1, which corresponds to the time scale for unsteady conduction inside the unburnt propellant.

Next, for the extended system, the optimum initial condition (V_{opt}) for the maximum transient growth is calculated. The state space vector $\chi(t)$ has N pairs of acoustic variables called 'acoustic modes'. The remaining $2N(M_g - 1)$ variables, called 'burn rate modes', describe the unsteady propellant burn rate response. Neither the acoustic modes nor the burn rate modes are the eigenmodes of the system. They are only reference modes (basis functions) satisfying the boundary condition and the variables are just projected along these modes.

The relative amplitude of various modes in the 'initial condition' (V_{opt}) is shown in figure 9 with the acoustic modes shown in the inset. The important observation is

https://doi.org/10.1017/S0022112010000133 Published online by Cambridge University Press

that, for obtaining maximum transient growth, one should also excite in the 'burn rate modes'. Although the appropriate response function (Y_R) is used instead of solving simultaneously the unsteady burn rate equations along with the acoustic equations, there is a huge difference in the transient growth between the two curves in figure 8(*a*). By using a response function, the dynamics involved in the unsteady burn rate are implicitly not taken into account. Now, if the optimum initial condition for the maximum transient growth is distributed more in the burn rate modes, then it is natural to expect a small transient growth, if the dynamics in the burn rate modes are not taken into account. Figure 9 shows indeed that the optimum initial condition is distributed among the burn rate modes, and hence there is a large difference in transient growth of both curves in figure 8(*a*). Therefore, for a stable system, according to the classical linear stability, a very small local change in propellant burn rate (might be due to inhomogeneity in the propellant) can give rise to an initial perturbation in the burn rate mode. Also, as the motor is fired initially, the temperature distribution is uniform in the propellant. As the SRM operates and as the port configuration changes as time evolves, after some time, there might be fluctuations in the temperature at the surface of the propellant. This serves as an initial condition where non-normality of the system plays a role. This can cause transient growth and the amplitude increases, eventually reaching a limit cycle (in the presence of nonlinearities). This important observation cannot be made if one uses the propellant response for modelling the burn rate, which neglects the transient dynamics of the burn rate response. Higher modes in both acoustics and burn rate do not contribute to the optimum initial condition showing the modal independence of the discretization with increasing number of modes (figure 9). The transient growth is shown to play an important role in pulsed instability, which is discussed below.

7.3. *Pulsed instability*

In SRMs, experiments indicate that rockets that are stable to small-amplitude disturbances become unstable for larger ones (Blomshield *et al.* 1997*b*). They then exhibit limit cycle oscillations or the rocket motor may be damaged. This phenomenon is known as 'pulsed instability' or 'triggering' (Culick 2006). From a dynamical system's point of view, this kind of phenomenon is termed as 'sub-critical transition' to instability. The system is linearly stable, but nonlinearly unstable. In the previous studies, only *ad hoc* models for burn rate–acoustic velocity coupling were used to simulate the experimental results (Wicker *et al.* 1996; Anathakrishnan *et al.* 2005; Flandro *et al.* 2007). Wicker *et al.* (1996) tried different forms of nonlinear propellant response functions Y_R to demonstrate triggering. Flandro *et al.* (2007) have given a comprehensive compilation of their earlier work and new formulations to predict the nonlinear stability of SRMs. However, their model also assumes an *ad hoc* propellant response function, which is not derived from the physics of the problem. Moreover, the coefficients in the forms of the *ad hoc* function are obtained from experiments (i.e. like matching limit cycle waveforms) and there is no rigorous theoretical reasoning behind them. This paper solves both acoustic and propellant response equations simultaneously, without any *ad hoc* assumptions on burn rate dependence on the acoustic field being made in the formulation. The present numerical simulations show 'pulsed instability' in some parameter range.

Pulsed instability can possibly occur in two ways. The first is when the initial disturbance amplitude is large enough for the nonlinear terms to be dominant compared with the linear terms right from the start of the evolution. The linearized equations (23), (24) and (25) are solved numerically and figure 10 shows decaying

https://doi.org/10.1017/S0022112010000133 Published online by Cambridge University Press

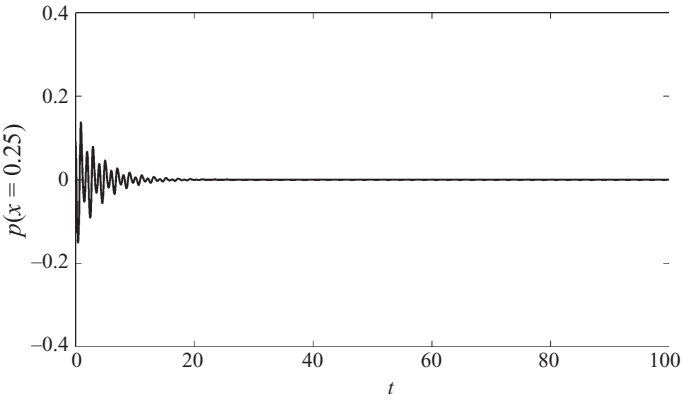


FIGURE 10. The evolution of acoustic pressure at $x = 0.25$ (linear simulation). $U_2(0) = 3$, $P_2(0) = 3, P_{m\neq 2}(0) = U_{m\neq 2}(0) = 0, MT_p(\eta = 1, 0) = 0.03, MT_p(\eta \neq 1, 0) = 0,\ C_1 = 0.02, C_2 = 0.02$.

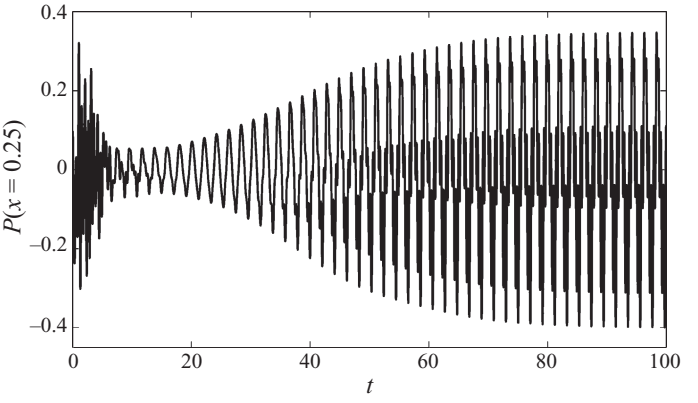


FIGURE 11. The evolution of acoustic pressure at $x = 0.25$ (nonlinear simulation). $U_2(0) = 3$, $P_2(0) = 3$, $P_{m\neq 2}(0) = U_{m\neq 2}(0) = 0$, $MT_p(\eta = 1, 0) = 0.03$, $MT_p(\eta \neq 1, 0) = 0$, $C_1 = 0.02$, $C_2 = 0.02$.

acoustic pressure oscillations. This means that the system is linearly stable. Linearized equations scale with initial conditions and the dynamical evolution will look similar for all scaled amplitudes. Now, for the same parameters and initial condition, the nonlinear terms are included and (15), (16) and (20) are solved. Figure 11 shows that the acoustic pressure initially decays, and after sometime it starts growing with the amplitude eventually reaching a limit cycle. The initial high-amplitude disturbance leads to the modal energy transfer from one mode to another by 'direct interaction' as explained in § 2. The energy transfer sustains the oscillations by keeping the disturbance energy among the modes, while in the linearized case, the energy can only get transferred to the base flow leading to the eventual decay of the acoustic oscillations. The same picture is shown in the phase space plot in figure 12. Figure 12 shows that the trajectory from the linear evolution ends in a stable focus showing classical linear stability. On the other hand, in figure 13, which is obtained from nonlinear simulation, the trajectory ends in a limit cycle eventually. A plot of acoustic energy (figure 14) shows that the linear and nonlinear simulations initially show a similar qualitative behaviour and after some time they both diverge, leading to a qualitatively different dynamical behaviour.

https://doi.org/10.1017/S0022112010000133 Published online by Cambridge University Press

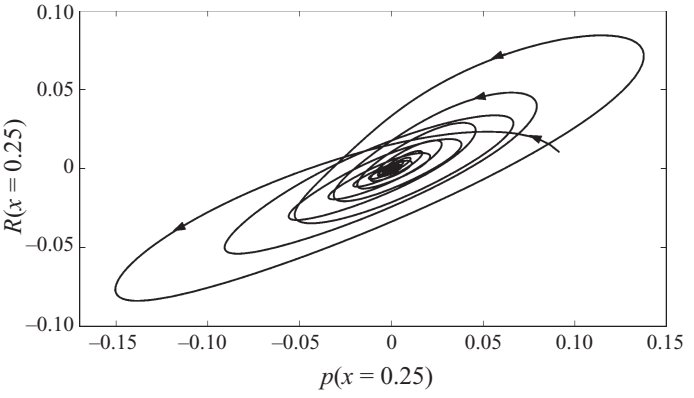


FIGURE 12. Phase portrait of the acoustic pressure and unsteady burn rate at $x = 0.25$ from the linear simulation. $U_2(0) = 3$, $P_2(0) = 3$, $P_{m\neq 2}(0) = U_{m\neq 2}(0) = 0$, $MT_p(\eta = 1, 0) = 0.03$, $MT_p(\eta \neq 1, 0) = 0$, $C_1 = 0.02$, $C_2 = 0.02$.

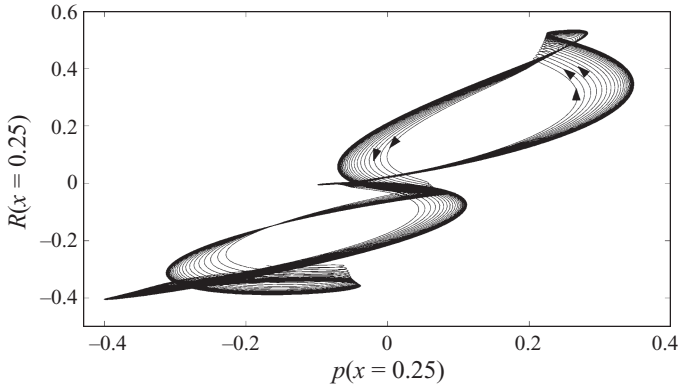


FIGURE 13. Phase portrait of the acoustic pressure and unsteady burn rate at $x = 0.25$ (near limit cycle) from the nonlinear simulation $U_2(0) = 3$, $P_2(0) = 3$, $P_{m\neq 2}(0) = 0$, $U_{m\neq 2}(0) = 0$, $MT_p(\eta = 1, 0) = 0.03$, $MT_p(\eta \neq 1, 0) = 0$, $C_1 = 0.02$, $C_2 = 0.02$.

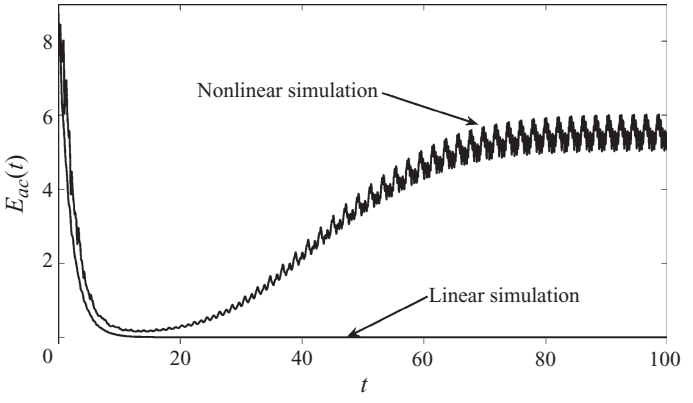


FIGURE 14. The evolution of acoustic energy $(E_{ac}(t) = \sum_{m=1}^{N} (U_m^2 + P_m^2))$ from linear and nonlinear simulations. $U_2(0) = 3$, $P_2(0) = 3$, $P_{m\neq 2}(0) = U_{m\neq 2}(0) = 0$, $MT_p(\eta = 1, 0) = 0.03$, $MT_p(\eta \neq 1, 0) = 0$, $C_1 = 0.02$, $C_2 = 0.02$.

https://doi.org/10.1017/S0022112010000133 Published online by Cambridge University Press

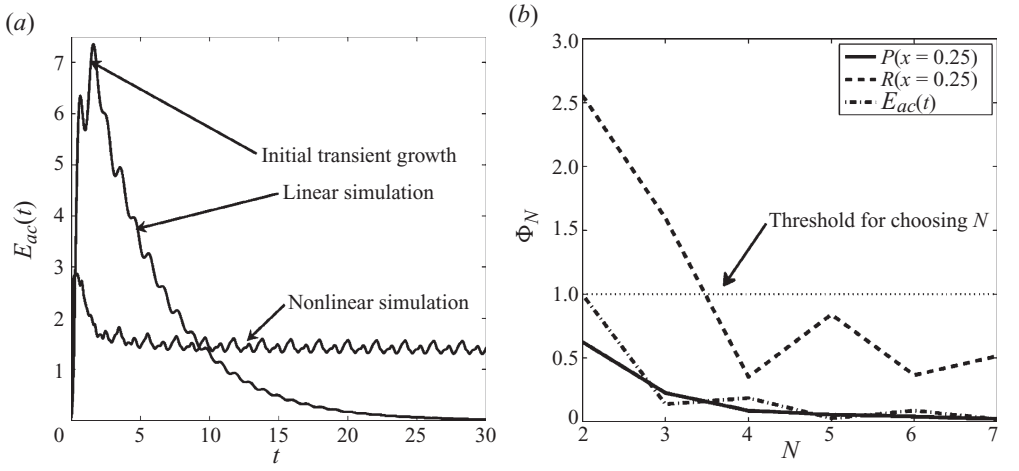


FIGURE 15. (*a*) The evolution of acoustic energy ($E_{ac}(t) = \sum_{m=1}^{N} (U_m^2 + P_m^2)$) with optimum initial condition $\chi(0) = V_{opt}$, $C_1 = 0.03$, $C_2 = 0.02$. (*b*) Convergence study for (*a*) with N. Note that $\Phi_N = \sqrt{\sum_{i=1}^{I} ((\phi_N(t_i) - \phi_{N-1}(t_i))/\phi_N(t_i))^2} \times 100$ is the measure used for studying the convergence of the simulations. Moreover, Φ_N represents any one of the variables $P(x = 1/4)$, $R(x = 1/4)$ and E. The summation index i represents the value of the variables at the ith time step in the numerical simulation. The threshold of Φ_N is chosen as 1 % for convergence of the solution, which corresponds to $N = 5$ in the present case.

The second route is by non-normal transient growth. Here even if one starts with a finite small-amplitude suitable initial condition, transient growth due to the non-normal nature of the system makes the oscillation grow even for a system stable according to linear stability theory. The transient growth leads to large-amplitude oscillations, which cause the nonlinear terms to play dominant roles and 'direct interaction' of eigenmodes occurs. Figure 15(*a*) shows the comparison of acoustic energy evolution with linear and nonlinear simulations. The transient growth in the linear simulation decays eventually, while the nonlinear simulation leads to a limit cycle. The higher transient growth in the linear simulation than that in the nonlinear one is due to the damping effect from the nonlinear terms. Here, the initial condition is chosen to be the optimum initial condition for the maximum transient growth ($\chi(0) = V_{opt}$) to show the importance of this route to triggering. Also note that the initial acoustic energy ($E_{ac}(t = 0) = 6.4 \times 10^{-4}$) is very small compared with that in figure 14 ($E_{ac}(t = 0) = 8.43$).

A convergence study is performed to evaluate the number of Galerkin modes used for the above simulations. Figure 15(*b*) shows the plot between percentage change (Φ_N) in the results of $P(x = 1/4)$, $R(x = 1/4)$ and E_{ac} for various values of N. It is found that for a threshold of 1 % change in the solution variables, $N = 5$ is sufficient. The non-dimensionalized dominant Fourier frequency of the acoustic pressure during the limit cycle corresponding to figure 15(*a*) is 0.48, which is very close to the fundamental frequency of a pipe, closed at both the ends. The non-dimensional frequency in figure 15(*a*) corresponds to 66.25 Hz for the SRM configuration given in table 1.

Transient growth is quantified in a particular measure (§ 4). In this paper, generalized disturbance energy $E_T(t)$ (defined to include the contribution of energy in the disturbance from the degrees of freedom associated with the unsteady burn rate, see

https://doi.org/10.1017/S0022112010000133 Published online by Cambridge University Press

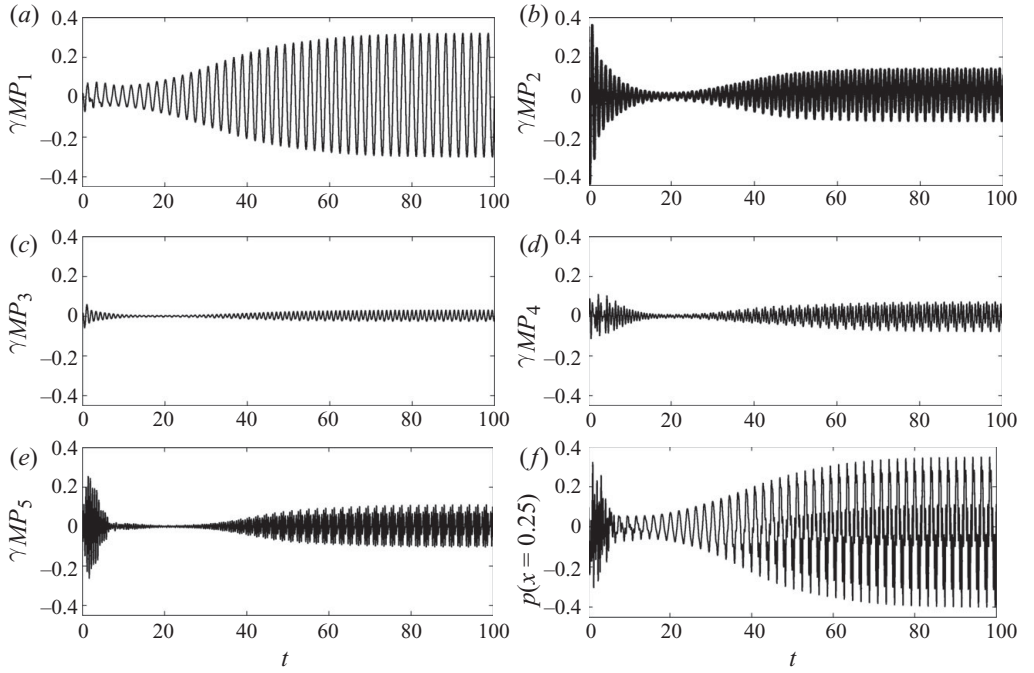


FIGURE 16. The evolution of Galerkin pressure modes: (*a*) first mode, (*b*) second mode, (*c*) third mode, (*d*) fourth mode, (*e*) fifth mode, (*f*) acoustic pressure at $x = 0.25$, $U_2 = 3.0$, $P_2 = 3.0$, $P_{m\neq 2}(0) = U_{m\neq 2}(0) = 0$, $MT_p(\eta, 0) = 0$, $C_1 = 0.02$, $C_2 = 0.02$.

§ 6) is used as a measure to quantify non-normality of the system. Transient growth from the present simulation can be observed and compared with the experiments, when $E_T(t)$ is measured. It is very difficult to devise an experiment to measure $E_T(t)$ in an SRM. The existing experiments with SRMs (Blomshield *et al.* 1997*a*, 1997*b*; Harris & Champlain 1998) measured only the acoustic pressure at the head end of the motor. Therefore, it is difficult to have one-to-one comparison of transient growth of thermoacoustic oscillations in SRMs from the available experimental acoustic pressure data with the present simulation.

7.4. *Bootstrapping*

Bootstrapping is a phenomenon where the dominant frequency of a system changes during the dynamical evolution of the system. This phenomenon is observed in SRMs (Yoon, Peddieson & Purdy 2001). Yoon *et al.* (2001) attributed this phenomenon to the nonlinearity alone. This is due to the transfer of energy among the modes by either nonlinear coupling or non-orthogonality of eigenmodes. The phenomenon of bootstrapping is discussed in the context of turbulence (Gebgart & Grossmann 1994) and thermoacoustic system (Yoon *et al.* 2001; Balasubramanian & Sujith 2008*a*, 2008*b*). An *ad hoc* acoustic velocity–combustion coupling model is used to simulate the observed behaviour in the Rijke tube (Yoon *et al.*; Balasubramanian & Sujith 2008*b*), whereas in Balasubramanian & Sujith (2008*a*), it comes by actually solving the unsteady equations for a ducted diffusion flame.

The initial condition ($t = 0$) is chosen as given in figure 16. The system, which is stable according to the classical linear stability theory, is excited in the second Galerkin mode, and the evolution of the other Galerkin modes is tracked. Figure 16(*a–e*) shows

https://doi.org/10.1017/S0022112010000133 Published online by Cambridge University Press

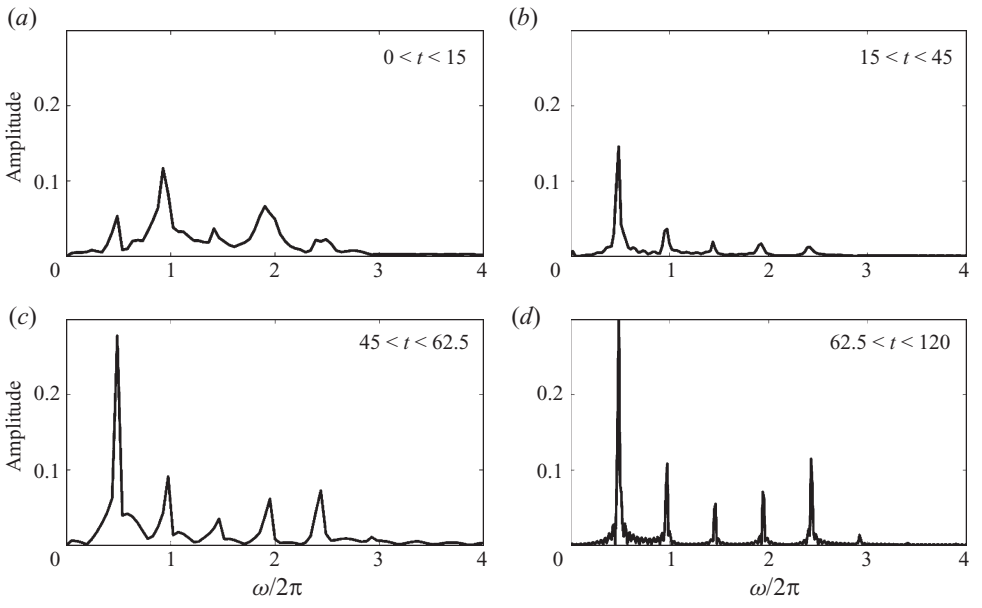


FIGURE 17. The Fourier transform of acoustic pressure at $x = 0.25$ during different time intervals, $U_2 = 3.0$, $P_2 = 3.0$, $P_{m\neq 2}(0) = U_{m\neq 2}(0) = 0$, $MT_p(\eta, 0) = 0$, $C_1 = 0.02$, $C_2 = 0.02$.

the evolution of the individual Galerkin pressure modes. Initially, the projection on the second mode decays and transfers the energy to the first mode (figure 16*a, b*). After some time, the first mode grows to sufficient extent, transferring the energy back to the second mode causing it also to grow.

The time evolution of acoustic pressure at $x = 0.25$ plotted in figure 16(*f*) shows that the pressure amplitude decreases initially and then, after some time, it increases by the modal energy transfer. The plot of the fast Fourier transform (FFT) of the acoustic pressure (figure 17) illustrates this phenomenon. For $0 < t < 15$, the second and fourth eigenmodes are the dominant ones, which decay as time evolves. In $15 < t < 45$, the first eigenmode grows because of the energy transfer from the second and fourth modes. Then, the first eigenmode transfers energy back to the second and fourth eigenmodes ($45 < t < 62.5$) causing them to grow again. In the end ($62.5 < t < 120$), there are higher harmonics due to the energy transfer to higher eigenmodes. The dominant frequencies present in the system in the limit cycle are close to the natural acoustic frequency of a closed–closed duct. A crucial difference is that the past analyses have demonstrated bootstrapping in acoustic velocity–combustion coupling systems (Yoon *et al.* 2001; Balasubramanian & Sujith 2008*a*, 2008*b*), whereas the present analysis used the acoustic pressure–combustion coupling model.

8. Conclusion

A thermoacoustic stability analysis of a solid rocket motor is performed with emphasis on the following. First, the non-orthogonality of the eigenmodes is accounted for by incorporating the mean flow (convection) effects in the acoustic equations. The classical linear stability theory predicts stability, which is valid only in the asymptotic time limit. For non-normal systems, the short-term behaviour can be completely different from the prediction by the classical linear stability theory for some initial conditions. The transient dynamics of the unsteady propellant burn rate are included

https://doi.org/10.1017/S0022112010000133 Published online by Cambridge University Press

instead of the *ad hoc* response models used in the earlier analysis. The acoustic and burn rate equations are solved simultaneously. In the present case, burn rate equations are solved for a homogeneous propellant. The inclusion of a differential equation in time for the unsteady burn rate leads to an increase in the degrees of freedom of the system. Therefore, the growth or decay of oscillations is quantified by a 'generalized disturbance energy', which includes the acoustic energy and the unsteady energy in the propellant. The same energy is related to the 2-norm of the state space vector that shows a transient growth because of the non-normal nature of the system. The optimum initial condition for maximum transient growth indicates a large contribution from the unsteady burn rate modes. The use of a burn rate response function would have not captured this observation because it neglects transients in burn rate modes. Using this model, exponential and pulsed instabilities are simulated. In the past, pulsed instability has been simulated only by using *ad hoc* response functions, which are not physics based. Moreover, in the present case, pulsed instabilities are simulated with burn rate pressure coupling as against the burn rate velocity coupling used in the earlier analysis. Pulsed instabilities can occur in two ways. First, by introducing a large pulse into the system where nonlinearities are important, leading to a limit cycle. Second, through a small initial condition in the appropriate direction that causes transient growth. As the amplitude of the oscillation increases, nonlinear terms can then contribute, leading to a limit cycle. Finally, other observed phenomena such as dominant frequency switching during the dynamical evolution of the system and 'bootstrapping' are also demonstrated. In summary, it is essential to include all the dynamics in the propellant response and the non-orthogonality of eigenmodes to predict instabilities more accurately in SRMs. The system is no longer purely acoustic, but an extended one with degrees of freedom in the combustion dynamics. The above analysis can be extended to other thermoacoustic systems that share a common feature.

This work was funded by the Indian Space Research Organization (technical monitors: Mr Jayaprakash and Dr M. S. Padmanabhan). The authors thank Priya Subramanian (IIT Madras) and K. Kedia (MIT Cambridge) for their suggestions and interesting discussions during the study.

Appendix A. Coupling terms in (10) and (11)

The linear and nonlinear coupling terms used in (10) and (11) are given below:

$$I^1_{n,m} = \int_0^1 \left[M\bar{U}\omega_m \cos(\omega_m x) + M\frac{\mathrm{d}\bar{U}}{\mathrm{d}x}\sin(\omega_m x) - k_m \sin(\omega_m x)\right] \sin(\omega_n x)\,\mathrm{d}x,$$

$$I^2_{n,m} = \int_0^1 \left(\frac{M^2\bar{U}}{\gamma}\frac{\mathrm{d}\bar{U}}{\mathrm{d}x}\cos(\omega_m x) - \omega_m \sin(\omega_m x)\right) \sin(\omega_n x)\,\mathrm{d}x,$$

$$I^3_{n,m} = -\int_0^1 k_m\bar{U}\cos(\omega_m x)\sin(\omega_n x)\,\mathrm{d}x,$$

$$I^4_{n,m} = -\int_0^1 k_m\bar{U}\sin(\omega_m x)\sin(\omega_n x)\,\mathrm{d}x,$$

$$I^5_{n,m} = \int_0^1 \gamma M\omega_m \cos(\omega_m x)\sin(\omega_n x)\,\mathrm{d}x,$$

$$I^6_{n,m} = \int_0^1 \left[(\lambda M)^2\frac{\mathrm{d}\bar{U}}{\mathrm{d}x}\bar{U}\cos(\omega_m x) - \gamma M^2\bar{U}\omega_m \sin(\omega_m x)\right] \cos(\omega_n x)\,\mathrm{d}x,$$

https://doi.org/10.1017/S0022112010000133 Published online by Cambridge University Press

$$I^7_{n,m} = -\int_0^1 k_e \cos(\omega_m x)\cos(\omega_n x)\,\mathrm{d}x,$$

$$N^1_n = \int_0^1 \left[\sum_{m=1}^{N}\left(R^c_m \cos(\omega_m x) + R^s_m \sin(\omega_m x)\right)\sum_{k=1}^{N} U_k \sin(\omega_k x)\right]\sin(\omega_n x)\,\mathrm{d}x,$$

$$N^2_n = \int_0^1 \left[\sum_{m=1}^{N} U_m \sin(\omega_m x)\sum_{k=1}^{N} U_k\omega_k \cos(\omega_k x)\right]\sin(\omega_n x)\,\mathrm{d}x,$$

$$N^3_n = \int_0^1 \left[\sum_{m=1}^{N} P_m \cos(\omega_m x)\sum_{k=1}^{N} P_k\omega_k \sin(\omega_k x)\right]\sin(\omega_n x)\,\mathrm{d}x,$$

$$N^4_n = \int_0^1 \left[\sum_{m=1}^{N} U_m \sin(\omega_m x)\sum_{k=1}^{N} P_k\omega_k \sin(\omega_k x)\right]\cos(\omega_n x)\,\mathrm{d}x,$$

$$N^5_n = \int_0^1 \left[\sum_{m=1}^{N} P_m \cos(\omega_m x)\sum_{k=1}^{N} U_k\omega_k \cos(\omega_k x)\right]\sin(\omega_n x)\,\mathrm{d}x.$$

Appendix B. Linearized equations

The linearized evolution equation for the coupled acoustic–burn rate equation is

$$\frac{\mathrm{d}\chi}{\mathrm{d}t} = L\chi \quad L = \begin{pmatrix} A_{2N\times 2N} & B_{2N\times(2N(M_g-1))} \\ C_{(2N(M_g-1))\times 2N} & D_{2N(M_g-1)\times 2N(M_g-1)} \end{pmatrix}_{(2NM_g)\times(2NM_g)},$$

$$A_{2N\times 2N} = -2\begin{pmatrix} I^1_{1,1} & I^2_{1,1} & I^1_{1,2} & I^2_{1,2} & \cdots \\ \frac{I^5_{1,1}}{\gamma M} & \frac{I^6_{1,1}}{\gamma M} - \frac{\alpha_{NO}+\xi_1}{2} & \frac{I^5_{1,2}}{\gamma M} & \frac{I^6_{1,2}}{\gamma M} & \cdots \\ I^1_{2,1} & I^2_{2,1} & I^1_{2,1} & I^2_{2,2} & \cdots \\ \frac{I^5_{2,1}}{\gamma M} & \frac{I^6_{2,1}}{\gamma M} & \frac{I^5_{2,1}}{\gamma M} & \frac{I^6_{2,2}}{\gamma M} - \frac{\alpha_{NO}+\xi_2}{2} & \cdots \\ & & & & \cdots \\ & & & & \cdots \\ & & & & \cdots \end{pmatrix}_{2N\times 2N},$$

$$B_{2N\times(2N(M_g-1))} = -\frac{2m}{\beta_1}\begin{pmatrix} E^c_{1,1} & E^c_{1,2} & \cdots & E^c_{1,N} & E^s_{1,1} & E^s_{1,2} & \cdots & E^s_{1,N} \\ E^c_{2,1} & E^c_{2,N} & \cdots & E^c_{2,N} & E^s_{2,1} & E^s_{2,1} & \cdots & E^s_{2,1} \\ \cdot & \cdot & \cdot & & & & & \\ & & & & & & \cdot & \\ & & & & & & \cdots & \cdot \end{pmatrix}_{2N\times(2N(M_g-1))},$$

https://doi.org/10.1017/S0022112010000133 Published online by Cambridge University Press

$E^c_{j,n}(1,1) = I^3_{j,n}$, $E^c_{j,n}(2,1) = I^7_{j,n}$, $E^s_{j,n}(1,1) = I^4_{j,n}$. All other entries are zero. Note that $E^c_{j,n}$ and $E^s_{j,n}$ are $2 \times (M_g - 1)$ matrices.

$$C_{(2N(M_g-1))\times 2N} = \begin{pmatrix} S_1 \\ S_2 \\ S_3 \\ . \\ . \\ S_N \\ 0 \\ 0 \\ 0 \\ . \\ . \end{pmatrix}_{(2N(M_g-1)\times 2N)} \qquad S_q(2,2) = \gamma M F \beta_1 \left(B(1-k) + \frac{2Bk}{\Delta\eta} \right),$$

S_q is $(M_g - 1) \times 2N$ matrix. All other entries are zero.

$$D_{2N(M_g-1)\times 2N(M_g-1)} = \begin{pmatrix} D^c & 0 \\ 0 & D^s \end{pmatrix} \quad D^s = D^c = \begin{pmatrix} G_1 & 0 & 0 & . & . \\ 0 & G_2 & 0 & . & . \\ & & . & & \\ & & & . & \\ 0 & 0 & . & . & G_N \end{pmatrix}_{(M_g-1)N\times(M_g-1)N},$$

$$G_N = F \begin{pmatrix} B^c_1 & 0 & B^c_2 & 0 & 0 & 0 & . & . \\ H^1_2 + H^4_2 & H^2_2 & H^3_2 & 0 & 0 & 0 & . & . \\ H^4_3 & H^1_3 & H^2_3 & H^2_3 & 0 & 0 & . & . \\ . & & & & & & & \\ . & & & & & & . & . \\ . & & & & & . & . & . \\ . & & & & & . & . & 0 \\ H^4_{Mg-1} & . & . & 0 & 0 & H^1_{Mg-1} & H^2_{Mg-1} & H^3_{Mg-1} \end{pmatrix}_{(M_g-1)\times(M_g-1)},$$

$$B^c_1 = A(k-1) - \left(\frac{k}{\Delta\eta}\right)^2 \left(1 + \frac{2\Delta\eta A}{k}\right) - m, \quad B^c_2 = \frac{\beta_1}{\beta_3}\left(\frac{k}{\Delta\eta}\right)^2,$$

$$H^1_q = \frac{\beta_i}{\beta_{i-1}} \left(\frac{k\eta_q - k^2\eta_q}{2\Delta\eta} + \left(\frac{k\eta_q}{\Delta\eta}\right)^2 \right), \quad H^2_q = -2\left(\frac{k\eta_q}{\Delta\eta}\right)^2,$$

$$H^3_q = \frac{\beta_i}{\beta_{i+1}} \left(\left(\frac{k\eta_q}{\Delta\eta}\right)^2 - \frac{k\eta_q - k^2\eta_q}{2\Delta\eta} \right), \quad H^4_q = -\frac{\beta_i}{\beta_1} m_p \eta_q^{1/k},$$

where η_q is the coordinate at qth discretized point. Note that $\Delta\eta$ is the same between all successive grid points.

REFERENCES

Anathakrishnan, N., Deo, S. & Culick, F. E. C. 2005 Reduced-order modeling and dynamics of nonlinear acoustic waves in a combustion chamber. *Combust. Sci. Tech.* **177**, 221–247.

Anderson, J. D. 1996 *Computational Fluid Dynamics*. Springer.

Anthoine, J., Buchlin, J. M. & Hirschberg, A. 2002 Effect of nozzle cavity on resonance in large SRM: theoretical modelling. *J. Propul. Power* **18**, 304–311.

https://doi.org/10.1017/S0022112010000133 Published online by Cambridge University Press

Baggett, J. S., Driscoll, T. A. & Trefethen, L. N. 1995 A mostly linear model of transition to turbulence. *Phys. Fluids* **7**, 833–838.

Balasubramanian, K. & Sujith, R. I. 2008*a* Non-normality and nonlinearity in combustion-acoustic interaction in diffusion flames. *J. Fluid Mech.* **594**, 29–57.

Balasubramanian, K. & Sujith, R. I. 2008*b* Thermoacoustic instability in a Rijke tube: non-normality and nonlinearity. *Phys. Fluids* **20**, 044103.

Barkley, D. & Tuckerman, L. S. 1999 Stability analysis of perturbed plane Coquette flow. *Phys. Fluids* **11**, 1187–1195.

Baum, J. D. & Levine, J. N. 1986 Modelling of nonlinear longitudinal instability in solid rocket motors. *AIAA J.* **13**, 339–348.

Blomshield, F. S., Mathes, H. B., Crump, J. E., Beiter, C. A. & Beckstead, M. W. 1997*a* Nonlinear stability testing of full-scale tactical motors. *J. Propul. Power* **13**, 349–355.

Blomshield, F. S., Mathes, H. B., Crump, J. E., & Beiter, C. A. 1997*b* Nonlinear stability testing of full scale tactical motors. *J. Propul. Power* **13**, 356–366.

Brewster, Q. & Son, S. F. 1995 Quasi-steady combustion modeling of homogeneous solid propellants. *Combust. Flame* **103**, 11–26.

Chu, B. T. 1965 On the energy transfer to small disturbances in fluid flow. *Acta Mech.* **1**, 215–234.

Cohen, N. S. & Strand, L. D. 1985 Combustion response to compositional fluctuations. *AIAA J.* **23**, 760–767.

Cozzi, F., Deluca, L. T. & Novozhilov, B. V. 1999 Linear stability and pressure-driven response function of solid propellants with phase transitions. *J. Propul. Power* **15**, 806–815.

Criminale, W. O. & Drazin, P. G. 2000 The initial-value problem for a modeled boundary layer. *Phys. Fluids* **12**, 366–374.

Crocco, L. 1956 Theory of combustion instability in liquid propellant rocket motors. *AGARDograph Rep* 0429886.

Culick, F. E. C. 1963 Stability of high-frequency pressure oscillations in rocket combustion chambers. *AIAA J.* **1**, 1097–1104.

Culick, F. E. C. 1968 A review of calculations for unsteady burning of a solid propellant. *AIAA J.* **6**, 2241–2255.

Culick, F. E. C. 1976*a* Nonlinear behaviour of acoustic waves in combustion chambers. Part I. *Acta Astronaut.* **3**, 715–734.

Culick, F. E. C. 1976*b* Nonlinear behaviour of acoustic waves in combustion chambers. Part II. *Acta Astronaut.* **3**, 735–757.

Culick, F. E. C. 1994 Some recent results for nonlinear acoustics in combustion chambers. *AIAA J.* **32**, 146–169.

Culick, F. E. C. 1997 A note on ordering perturbations and the insignificance of linear coupling in combustion instabilities. *Combust. Sci. Tech.* **126**, 359–379.

Culick, F. E. C. 2006 Unsteady motions in combustion chambers for propulsion systems. *RTO AGARDograph* AG-AVT-039.

Culick, F. E. C., Burnley, V. & Swenson, G. 1995 Pulsed instabilities in solid-propellant rockets. *J. Propul. Power* **11**, 657–665.

Culick, F. E. C. & Isella, G. 2000 Modelling the combustion response function with surface and gas phase dynamics. In *Thirty-Eighth Aerospace Sciences Meeting and Exhibit. AIAA Paper* 2000-0310.

Deluca, L., Disilvestro, R. & Cozzi, F. 1995 Intrinsic combustion instability of solid energetic materials. *J. Propul. Power* **11**, 804–815.

Farrell, B. F. & Ioannou, P. J. 1996 Generalized stability theory. Part I. Autonomous operators. *J. Atmos. Sci.* **53**, 2025–2040.

Flandro, G. A. 1995*a* Effects of vorticity on rocket combustion stability. *J. Propul. Power* **11**, 607–625.

Flandro, G. A. 1995*b* On flow turning. In *Thirty-First ASME, SAE, and ASEE, Joint Propulsion Conference and Exhibit. AIAA Paper* 1995-2730

Flandro, G. A. 1996 Nonlinear combustion instability data reduction. In *Thirty-Second AIAA/ASME/SAE/ASEE Joint Propulsion Conference and Exhibit. AIAA Paper* 1996-3251.

Flandro, G. A., Fischbach, S. R. & Majdalani, J. 2007 Nonlinear rocket motor stability prediction: limit amplitude, triggering and mean pressure shift. *Phys. Fluids* **19**, 094101.

https://doi.org/10.1017/S0022112010000133 Published online by Cambridge University Press

Flandro, G. A. & Majdalani, J. 2003 Aeroacoustic instability in rockets. *AIAA J.* **41**, 485–497.

Friedly, J. C. & Petersen, E. E. 1966 Influence of combustion parameters on instability in solid propellant motors. Part I. Development of model and linear analysis. *AIAA J.* **4**, 1604–1610.

Gebgart, T. & Grossmann, S. 1994 Chaos transition despite linear stability. *Phys. Rev.* E **50**, 3705–3711.

Golub, G. H. & Van Loan, C. E. 1989 *Matrix Computations*. The Johns Hopkins University Press.

Gusachenko, L. K. & Zarko, V. E. 2008 Analysis of unsteady solid-propellant combustion models (review). *Combust. Explo. Shock Waves* **44**, 31–42.

Harris, P. G & Champlain, A. D. 1998 Experimental database describing pulse-triggered nonlinear instability in solid rocket motors. *J. Propul. Power* **14**, 429–439.

Junye, W. 2000 Non-linear analysis of solid propellant burning rate behaviour. *Intl J. Numer. Methods Fluids* **33**, 627–640.

Kedia, K. S., Nagaraja, S. B. & Sujith, R. I. 2008 Impact of linear coupling on thermoacoustic instabilities. *Combust. Sci. Tech.* **180**, 1588–1612.

Krasnov, D. S., Zienicke, E., Zikanov, O., Boeck, T. & Thess, A. 2004 Numerical study of the instability of the Hartmann layer. *J. Fluid Mech.* **504**, 183–211.

Krier, H., T'ien, S. J., Sirignana, W. A. & Summerfield, M. 1968 Nonsteady burning phenomena of solid propellants: theory and experiments. *AIAA J.* **6**, 278–285.

Kumar, K. R. & Lakshmisha, K. N. 2000 Nonlinear intrinsic instability of solid propellant combustion including gas-phase thermal inertia. *Combust. Sci. Tech.* **158**, 135–166.

Kuo, K. K. & Summerfield, M. 1984 Fundamentals of solid-propellant combustion. *Prog. Astronaut. Aeronaut.* **90**, 760–767.

Kourta, A. 1997 Shear layer instability and acoustic interaction in solid propellant rocket motors. *Intl J. Numer. Methods Fluids* **25**, 973–981.

Lee, J. G. & Santavicca, D. A. 2005 Experimental diagnostics of combustion instabilities. *Prog. Astronaut. Aeronaut.* **210**, 481–529.

Levine, J. N. & Baum, J. D. 1983 A numerical study of nonlinear instability phenomena in solid rocket motors. *AIAA J.* **21**, 557–564.

Lin, A. C. & Wang, S. Y. 1995 Investigation of aluminized solid propellant combustion instability by means of a T-burner. In *Thirty-Third Aerospace Sciences Meeting and Exhibit. AIAA Paper* 95-0606.

Margolis, S. B. & Armstrong, R. C. 1986 Two asymptotic models for solid propellant combustion. *Combust. Sci. Tech.* **47**, 1–38.

Margolis, S. B. & Armstrong, R. C. 1988 Diffusional/thermal coupling and intrinsic instability of solid propellant combustion. *Combust. Sci. Tech.* **59**, 27–84.

Matveev, K. I. 2003 Thermo-acoustic instabilities in the Rijke tube: experiments and modeling. PhD thesis, California Institute of Technology.

Mukhopadhyay, B., Afshordi, N. & Narayan, R. 2006 Growth of hydrodynamic perturbations in accretion disks: possible route to non-magnetic turbulence. *Adv. Space Res.* **38**, 2877–2879.

Nagaraja, S. B., Kedia, K. S. & Sujith, R. I. 2009 Characterizing energy growth during combustion instabilities: singular values or eigenvalues? *Proc. Combust. Inst.* **39**, 2933–2940.

Nicoud, F., Benoit, L., Sensiau, C. & Poinsot, T. 2007 Acoustic modes in combustors with complex impedances and multidimensional active flames. *AIAA J.* **45**, 426–441.

Padmanabhan, M. S. 1975 The effect of nozzle nonlinearities on the nonlinear stability of liquid rocket motors. PhD thesis, Georgia Institute of Technology, Atlanta, USA.

Price, E. W. 1984 Fundamentals of solid-propellant combustion. *Prog. Astronaut. Aeronaut.* **90**, 479–513.

Reddy, S. C. & Trefethen, L. N. 1994 Pseudospectra of the convection–diffusion operator. *SIAM J. Appl. Maths* **54**, 1634–1639.

Rienstra, S. W. & Hirschberg, A. 2008 An introduction to acoustics. *IWDE Rep.* 92-06.

Riley, K. F., Hobson, M. P. & Bence, S. J. 2006 *Mathematical Methods for Physics and Engineering*. Cambridge University Press.

Romanov, O. Y. 1999 Unsteady burning of solid propellants. *J. Propul. Power* **15**, 823–836.

Schmid, P. J. 2007 Nonmodal stability theory. *Annu. Rev. Fluid Mech.* **39**, 129–162.

Schmid, P. J. & Henningson, D. S. 2001 *Stability and Transition in Shear Flows*. Springer.

https://doi.org/10.1017/S0022112010000133 Published online by Cambridge University Press

Shimada, T., Hanzawa, M., Kata, T., Yoshikawa, T. & Wada, Y. 2007 Stability analysis of solid rocket motor combustion by computational fluid dynamics. In *Thirteenth AIAA/CEAS Aeroacoustics Conference. AIAA Paper* 2007-3427.

Strogatz, S. H. 2001 *Nonlinear Dynamics and Chao: With Applications to Physics, Biology, Chemistry and Engineering*. Perseus Books.

Sutton, G. P. 2001 *Rocket Propulsion*. Wiley-IEEE.

Trefethen, L. N. & Embree, M. 2005 *Spectra and Pseudospectra: The Behaviour of Nonnormal Matrices and Operators*. Princeton University Press.

Vuillot, J. 1995 Vortex shedding phenomena in solid rocket motors. *J. Propul. Power* **11**, 626–639.

Ward, M. J., Son, S. F. & Brewster, M. Q. 1998 Steady deflagration of HMX with simple kinetics: a gas phase chain reaction model. *Combust. Flame* **114**, 556–568.

Wicker, J. M., Greene, W. D., Kim, S.-I. & Yang, V. 1996 Triggering of longitudinal combustion instabilities in rocket motors: nonlinear combustion response. *J. Propul. Power* **12**, 1148–1158.

Williams, F. A. 1962 Response of a burning solid to small-amplitude pressure oscillations. *J. Appl. Phys.* **33**, 3153–3166.

Williams, F. A. 1985 *Combustion Theory*. Addison-Wesley.

Yang, V., Kim, S. I. & Culick, F. E. C. 1990 Triggering of longitudinal pressure oscillations in combustion chambers. Part I. Nonlinear gasdynamics. *Combust. Sci. Tech.* **72**, 183–214.

Yoon, H. G., Peddieson, J. & Purdy, K. R. 2001 Non-linear response of a generalized Rijke tube. *Intl J. Engng Sci.* **39**, 1707–1723.

Zinn, B. T. 1972 Longitudinal mode acoustic losses in short nozzles. *Res. Rep.* AD0744623. Naval Weapons Center China Lake.

Zinn, B. T. & Lores, M. E. 1971 Application of the Galerkin method in the solution of nonlinear axial combustion instability problems in liquid rockets. *Combust. Sci. Tech.* **4**, 269–278.

https://doi.org/10.1017/S0022112010000133 Published online by Cambridge University Press